Methodology for Monitoring Silting and the Coastline of Small Ports Using Sentinel-2 Images: The Case of Port Cap Djinet Algeria

Hocine Dahmani, Fouzia Houma Bachari, François Marin, Nour Islam Bachari

remote sensing

MDPI

Article

Methodology for Monitoring Silting and the Coastline of Small Ports Using Sentinel-2 Images: The Case of Port Cap Djinet Algeria

Hocine Dahmani [1,*], Fouzia Houma Bachari [1], François Marin [2] and Nour Islam Bachari [3]

[1] Laboratory of Marine and Coastal Ecosystems (ECOSYSMarL), Higher National School of Marine Sciences and Coastal Management, University Campus Dely Ibrahim, Bois des Cars, PB 19, Algiers 16320, Algeria; fouzia.houma.bachari@enssmal.edu.dz
[2] Laboratory of Waves and Complex Media (LOMC), Le Havre Normandy University, UMR 6294 CNRS, 76600 Le Havre, France; francois.marin@univ-lehavre.fr
[3] Laboratory of Biological Oceanography and Marine Environment (LOBEM), Faculty of Biology, University of Sciences and Technology Houari Boumediene, BP 32 El-Alia Bab Ezzouar, Algiers 16111, Algeria; nbachari@usthb.dz
* Correspondence: hocine.dahmani@enssmal.edu.dz

Abstract: One of the ports most affected by the phenomenon of silting in Algeria is the port of Cap Djinet. In order to consider the monitoring of this port over a period of 8 years between 2015 and 2023, the twin Sentinel-2 A/B satellites were used. After image pre-processing, the bathymetry was estimated using the algorithm developed by Stumpf and extraction of the coastline was conducted using the normalized difference water index (NWDI). As part of this work, four bathymetric surveys were conducted in situ in four different periods, the results of which then correlated with those of the Stumpf model applied to satellite images. The results of the regression analysis are consistent and show good correlation coefficients (R^2) between 0.67 and 0.80 and root-mean-square error (RMSE) values between 0.87 m and 1.32 m, except for images captured under turbid water conditions. The maximum accretion surface is 2.12 ha to the north of the port, estimated for the period from 2018 to 2019, and 1.78 ha to the south for 2015 to 2016. The maximum erosion surface is 2.37 ha to the north of the port for the period from 2017 to 2018 and 1.16 ha to the south from 2017 to 2018. Therefore, the amplitude of accretion and erosion is greater to the north of the port than to the south. The present study demonstrates the ability of Sentinel-2 satellites to monitor silting and coastline changes in the vicinity of this port, which could help to address the effects of climate change and human activities in order to protect the marine ecosystem.

Keywords: silting; Cap Djinet port; Sentinel-2; bathymetry; accretion; erosion; Stumpf method; SDB (satellite-derived bathymetry); NDWI (normalized difference water index)

Citation: Dahmani, H.; Bachari, F.H.; Marin, F.; Bachari, N.I. Methodology for Monitoring Silting and the Coastline of Small Ports Using Sentinel-2 Images: The Case of Port Cap Djinet Algeria. *Remote Sens.* **2024**, *16*, 2764. https://doi.org/10.3390/rs16152764

Academic Editor: Javier Marcello

Received: 26 May 2024
Revised: 16 July 2024
Accepted: 23 July 2024
Published: 29 July 2024

1. Introduction

The problem of the silting up of ports is related to their basic function, and in particular, the provision of shelter by creating conditions of quiescence [1]. Generally, ports are exposed to the risk of silting as they shelter not only boats but also sediments. Indeed, ports built on sandy coastal areas receive sand mainly from the littoral drift activated by oblique incident waves [2]. The main mechanisms responsible for sedimentation have been widely reported in scientific journals [3–6]. Waves and currents play an important role in the suspension of sediments in shallow coastal waters [7], with waves being locally generated by wind or propagating from the open sea, while currents are partially generated by tides, wind, and density gradients [8].

At present, around 15% of the old Mediterranean ports are silted up, with around 75% of these ports being out of service [2]. Algeria belongs to the Mediterranean basin

and has a coastline of nearly 1300 km [9]. In order to better explore the country's fishing resources, the government has built numerous fishing ports along the coast. Unfortunately, a number of these ports are already exposed to sedimentation issues, which could be due to their poor design. One of the fishing ports which suffers from this problem is the port of Cap Djinet in Boumerdes. Since its construction in 2006, this port has been widely studied by engineers and scientists in recent years, in order to characterize and manage this area effectively [10,11], but without recourse to continuous technical monitoring such as marine remote sensing and historical satellite imagery [12]. For all fishing port construction projects in Algeria, engineers from the Laboratoire Etudes Maritimes LEM in 2009 used a numerical sediment transport model—namely, the MIKE 21 tool with validation by physical modeling—including for the Port of Cap Djinet. According to satellite images from 2002 to 2023 (Figure 1), this port silted up just after the commissioning of the project in 2009.

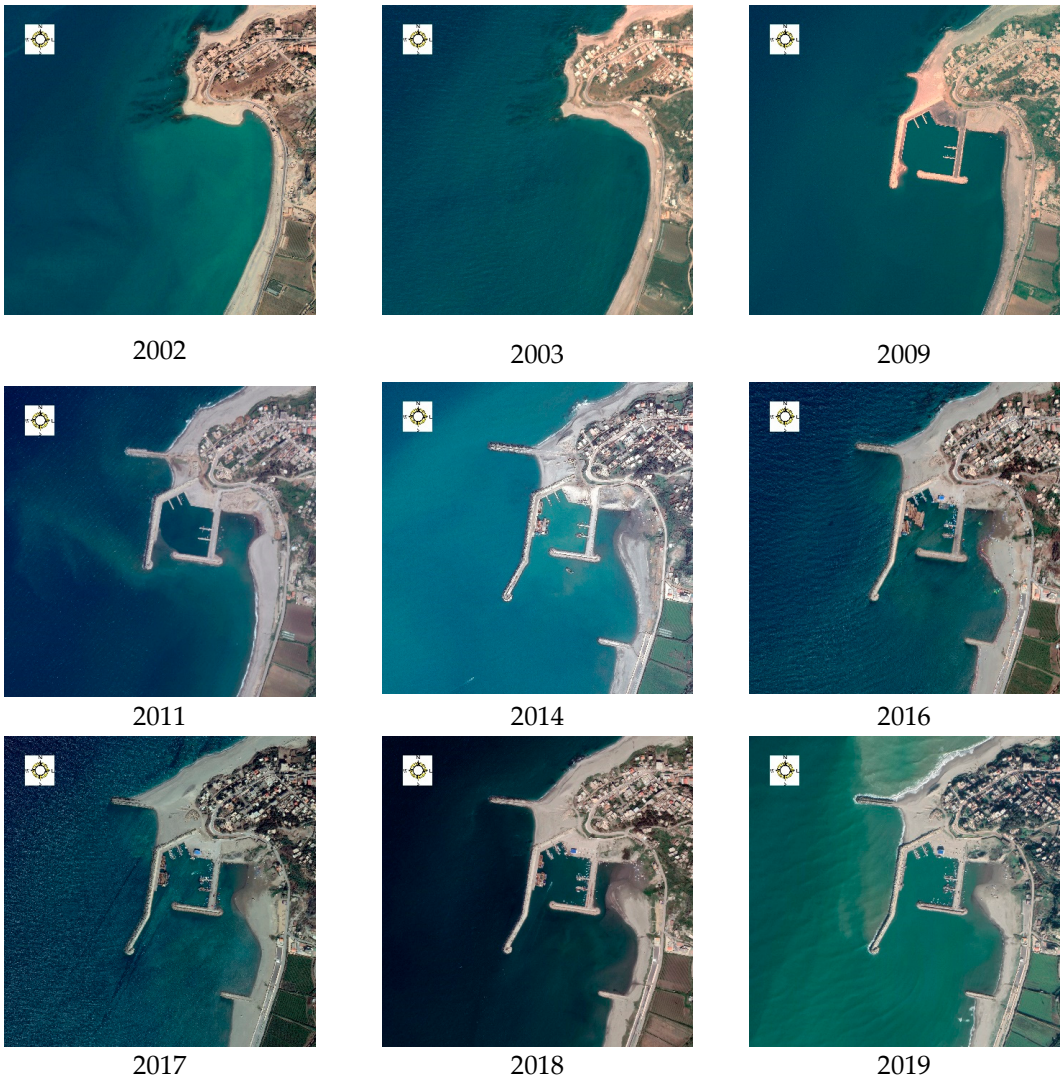

Figure 1. *Cont.*

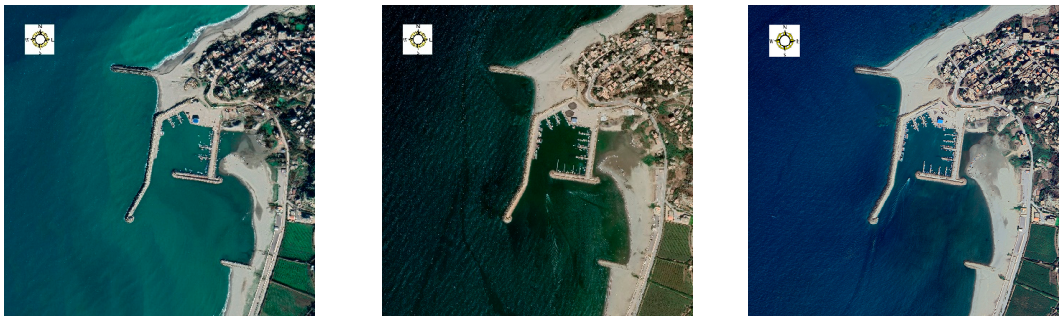

Figure 1. Satellite images from 2002 to 2023 showing coastal accretion and erosion trend [13].

In order to monitor harbor silting, it is necessary to understand and evaluate the coastal sediment transport, particularly near areas of accretion and erosion, as well as near sand spits. For the management of coastal erosion zones, a better understanding of the morphological changes is necessary [14]. Additionally, better monitoring is needed to evaluate the different possible scenarios, particularly to determine the spatio-temporal variability of the closure of sand spits [12,15]

The current situation of the port of Cap Djinet and its surroundings requires a very efficient and real-time method for monitoring the silting problem. The traditional monitoring method, using in situ measurements of bathymetric surveys carried out periodically, is costly in terms of time, effort, and human and material resources, especially when it involves a large study area and long-term management design. To facilitate spatio-temporal analyses over a large area, remote sensing technologies must be integrated into large-scale studies. With the rapid advancement of satellite and aerial vehicle technologies, large-scale remote sensing image retrieval has recently become an important research question in the geoscience field [16].

Concerning the remote sensing-based retrieval of sediment properties, including sedimentation rates, there is generally consistency between field and laboratory measurements, indicating that the proposed methodology will have important implications in engineering, environmental, and coastal management contexts [17].

Remote sensing data and GIS (Geographic Information System) methods could provide valuable estimates of coastline variability, allowing for the quantification of historical rates of change and determining the processes that have affected coastlines [18]. Satellite images are particularly useful for shoreline and coastal monitoring and management [19], obtained through open-access programs where the data are available.

The European Copernicus program is the program for Earth observation issued from the European Commission and the European Space Agency ESA [20,21]. The data and images from Sentinel satellites obtained through this program are freely accessible. The Sentinel-2 satellite is based on a constellation of two identical satellites—Sentinel-2A and Sentinel-2B—which were launched separately, and offers high- and medium-resolution images (10–60 m) with 5-day repetitive coverage [22,23]. As such, it constitutes a useful tool for studying coastal processes [24,25].

These satellites are equipped with a multi-spectral instrument (MSI) featuring 13 spectral bands ranging from visible spectrum (VIS) and near-infrared (NIR) to shortwave infrared (SWIR) at different spatial scales. They are useful for sea–land mapping [12,26]. Imagery data processing is widely conducted using the Arcgis, Qgis, Envi, Google Earth Engine (GEE), and SNAP software [27]. The European Space Agency (ESA) developed three free and open-source toolkits for the scientific operation of the Sentinel-1, Sentinel-2, and Sentinel-3 missions. These tools are based on a common software platform, namely the satellite imagery processing application by the SNAP Sentinel Application Platform, and can be used for the processing and management of georeferenced geospatial data [28].

Several research works have been carried out using the Sentinel-2 satellite and the SNAP platform in coastal and marine areas, for example, for the assessment and monitoring of coastal water quality [29,30], detection of oil spills in the sea [31], environmental management, and understanding and mitigation of the effects of climate change [32].

Several empirical algorithms for satellite-derived bathymetry (SDB) are available in the literature, such as those described in [33,34], as well as analytical algorithms [35–38]. The mapping of port bathymetry and the monitoring of marine sediment transport using Sentinel-2 satellite imagery can be used for coastal management research [39,40]. Remote sensing data can be used effectively to monitor changes along the coastal zone, including the shoreline, with reasonable precision [41]. The authors of [42] showed that it is possible to determine the bathymetry in the case of shallow water, and the suspended matter in suspension from satellite images if the topography of the area is known.

The integrated sea–land approach is a tool for the presentation of the sediment distribution, including coastal deposit areas [43]. Sea–land segmentation is an essential remote sensing task for various coastal and environmental studies, such as shoreline mining, coastal erosion and accretion, and coastal zone monitoring [44]. Although water indices allow for distinguishing water from land, it is difficult to identify the different types of water solely by the value of the index [45]. The normalized difference water index (NDWI) has been used for land/sea separation [46].

Numerous studies have been carried out on the use of the NDWI and modified NDWI (MNDWI) [47], with the NDWI initially developed for applications to Landsat Thematic Mapper TM images [46], while the MNDWI index was developed for application in urbanized areas [48]. Moreover, the NDWI index is better for research on the evolution of coasts and coastlines [49]. Several researchers have succeeded in using the contour and threshold detection method on NDWI data for the delimitation of coastlines [50–55].

The present work deals with a selection of Sentinel A and B imagery to monitor silting and the evolution of the coastline in the vicinity of the port of Cap Djinet over a period of 8 years (from 2015 to 2023). Atmospheric and radiometric corrections of Sentinel-2 images were carried out using the SNAP 9.0.0 software. The application of the Stumpf algorithm and the SNAP NDWI to these images make it possible to follow both the change in the bathymetry through altimetry (in 3D) and the spatio-temporal variation of the coastline (in 2D). In order to assess the variation in bathymetry in the port of Cap Djinet, in situ water depth measurements using an echosounder were correlated with the reflectance results of the images in the blue (B2) and green (B3) bands of the Stumpf log-transformed band ratio model algorithm for four different periods. Mapping the coastline using the NDWI over multi-year periods makes it possible to locate and estimate the surfaces of accretion and erosion zones.

2. Materials and Methods

2.1. Study Site

The fishing port of Cap Djinet (36°52′10″–36°52′45″N, 3°42′25″–3°43′40″E) is located about 80 km east of Algiers, at the eastern end of Zemmouri Bay, and less than 20 km west of the town of Dellys (Figure 2). This port was built on a sandy coast and has two jetties and two groynes. The main jetty is 580.0 m long, while the secondary jetty is 340.0 m long. One 280 m long groyne is located to the north and the other groyne (150 m long) is located to the south.

Along the coast, there is an elongated beach which extends from the mouth of Wadi Isser to the west and to that of Wadi Sebaou on the east side. This area is also characterized by coastal sediment transport fed by several watercourses: the large wadis Isser and Sebaou, and the smaller wadis Laamara and Arbaâ with their small dams.

During the 1990s, the coastline of Cap Djinet on the west side suffered from remarkable erosion of the beach, threatening the integrity of national road number 24. A site protection study was drawn up by the Algerian Maritime Design Laboratory in 1992, according to the LEM in 2009.

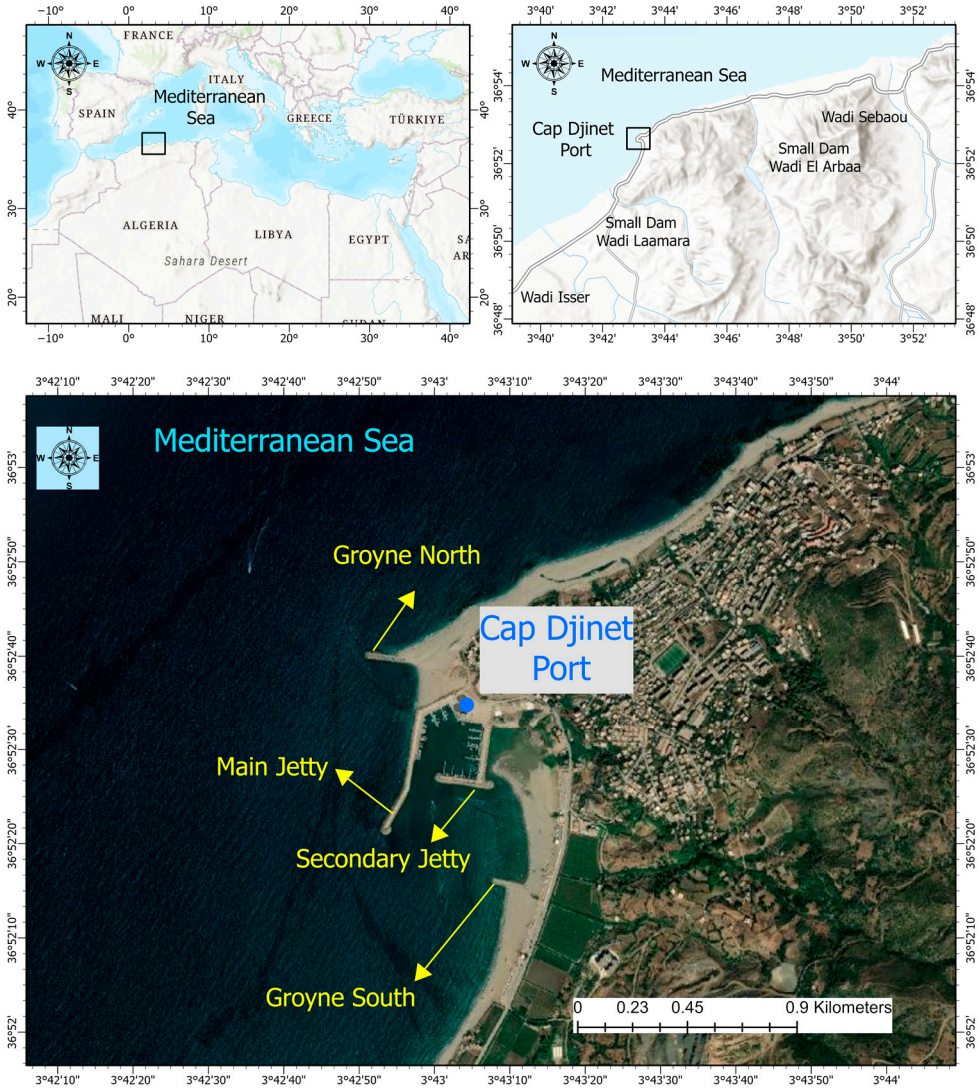

Figure 2. Study area: Cap Djinet Port.

2.2. In Situ Bathymetry Data

As part of our work, in order to measure the water depth, an ODOM ECHOTRAC echosounder with a resolution of 0.01 m was used with the Trimble 5700 GPS receiver (made in country united states) and a GARMIN 76C type pocket GPS (made in country united states) to follow the location of the sampling points using an inflatable boat. The geodetic reference system suitable for GPS is WGS84 Universal Transverse Mercator (UTM) projection zone 31 north, the altimeter heights are in meters, and the marine environment is up to the zero of the Algerian levelling system N.G.A (Nivellement General de L'Algerie).

The precision of in situ water depth measurements is very important when using an empirical model [56]. Therefore, calibration of the echosounder required the use of a metal plate suspended with a graduated chain. The plate was immersed at a chosen depth in relation to the level of the body of water. The calibration was performed by acting on the signal propagation speed in water in order to obtain a depth displayed on the echosounder which is equal to that read on the chain's graduations. The data acquired during the bathymetry survey were processed using HYPACK v18.1.18 software. This treatment consisted of deleting the probes resulting from false measurements. It should be noted that the data points taken physically at a depth of less than −20 m were used as validation data.

The water depths were recorded in four periods between 2020 and 2022: 12 August 2020, 5 January 2021, 14 August 2022, and 27 December 2022. During the measurement campaigns, we planned measurement points both for calibration and validation of the regression model. After processing the data by filtering and removing gap points, a summary of the measurement points was developed, as shown in Table 1 below. This table presents the number of calibration and validation points measured in the port of Cap Djinet, as well as the maximum and minimum depths according to the in situ measurement dates.

Table 1. Depths and numbers of calibration and validation measurement points in the study area according to in situ measurement dates.

Port	Dates	In Situ Depths					
		Calibration Points			Validation Points		
		Number of Data Points	Max Depth [m]	Min Depth [m]	Number of Data Points	Max Depth [m]	Min Depth [m]
Cap Djinet	12 August 2020	270	−8.00	−0.90	62	−7.30	−2.32
	5 January 2021	78	−7.60	−1.00	23	−7.10	−1.23
	14 August 2022	250	−9.70	−0.60	82	−7.18	−0.80
	27 December 2022	651	−19.30	−0.50	136	−17.90	−1.33

2.3. Sentinel-2 Satellite Imagery

The port of Cap Djinet is a local area with a great variability in sediment transport, which requires high short-term spatio-temporal resolution; thus, the two S2-A/B satellite products were used. The products (i.e., 100 × 100 km^2 orthoimages in the UTM/WGS84 projection which were extracted from a single orbit) were manually reviewed according to the thumbnail on the product download website [57]. In this study, the Sentinel-2 MSI Level-1C (L1C) and Sentinel-2 MSI Level-2A (L2A) products were used. The L1C is a radiometrically and geometrically corrected image containing an orthorectified image of the reflectance at the top-of-atmosphere (TOA). The L2A is an atmospherically corrected orthoimage, comprising a bottom-of-atmosphere (BOA) surface reflectance product [58].

Sentinel-2 includes a constellation of two identical satellites situated at the same orbit but 180° apart, which allows for an overall maximum visit time of 5 days. Sentinel-2A was launched on 23 June 2015 from Kourou, French Guiana, at mean local solar time (10:30 a.m.), while Sentinel-2B was launched on 7 March 2017. These dates indicate the limit of possible retrospective analyses. Table 2 below shows the original Sentinel-2 bands with their respective central wavelengths [59]. The bands have a spatial resolution of 10–60 m. For example, the resolution of B2, B3, B4, and B8 is 10 m, whereas that of B5, B6, B7, B8A, B11, and B12 is 20 m. The resolution of the remaining bands is 60 m (Table 2).

Table 2. Sentinel-2 bands with their respective central wavelengths and spatial resolutions.

Number of Band	Name	Central Wavelength (m)	Spatial Resolution (m)
B1	Coastal aerosol	443	60
B2	Blue	490	10
B3	Green	560	10
B4	Red	665	10
B5	Red—edge 1	705	20
B6	Red—edge 2	740	20
B7	Red—edge 3	783	20

Table 2. *Cont.*

Number of Band	Name	Central Wavelength (m)	Spatial Resolution (m)
B8	NIR	842	10
B8A	NIR narrow	865	20
B9	Water vapor	945	60
B10	Cirrus	1375	60
B11	SWIR 1	1610	20
B12	SWIR 2	2190	20

It should be noted that there are temporal differences in the data collection. The Sentinel-2 data set was selected due to its temporal proximity to the bathymetry measurement dates presented previously and the availability of cloud-free data. Sentinel-2 L2A images were collected in four periods, according to Table 3.

Table 3. Dates of acquisition of Sentinel-2 data.

Dates of Acquisition	Sentinel-2 Image Reference (A and B/L2A)
7 August 2020	S2B_MSIL2A_20200807T102559_N0214_R108_T31SEA_20200807T132026
4 January 2021	S2B_MSIL2A_20210104T103329_N0214_R108_T31SEA_20210104T131305
12 August 2022	S2A_MSIL2A_20220812T103031_N0400_R108_T31SEA_20220812T182800
25 December 2022	S2B_MSIL2A_20221225T103349_N0509_R108_T31SEA_20221225T131936

2.4. Methodology

Satellite bathymetry represents a passive technology which measures solar radiation intensity, unlike in situ water depth measurements using an echosounder [60]. For our study, we used the Sentinel-2 Level-2A products detected in the study period, including products with 0% to 5% cloud cover (according to the Figure 3). Therefore, the L2A data sets with atmospheric correction applied were selected, which allows for a faster geo-processing workflow and better application of normalized indices.

Sentinel Application Platform (SNAP 9.0.0) software was used for image processing. Concerning the second step, re-sampling of all Sentinel-2 bands was carried out using a reference band with a spatial resolution of 10 m (example B2). As the tiles of Sentinel-2 are large (100 × 100 km^2), and to facilitate processing, we sub-selected the product according to our study area, "port of Cap Djinet", using the Subset tool. The third step consisted of correcting sun glint on all images. Sun glint is a common phenomenon in satellite images, which essentially refers to the specular reflection of the sun on water surfaces. The water-leaving reflectance can be difficult to observe due to the reflection of direct sunlight on the air–water interface (sun glint) in the direction of the satellite. The viewing geometry of the Sentinel-2 satellite makes it vulnerable to sun glint contamination. In the presence of sun glint, a glint removal algorithm must be applied in order to be able to observe the sea floor for the purpose of habitat mapping or bathymetry derivation. There are several available sun glint removal methods for high-resolution images and coastal applications. The algorithm implemented as part of the Sen2Coral toolbox was developed using Equation (1), as described in [61]. While the algorithm gives reasonably good results, it is still recommended to use images with minimal glint.

$$R'_i = R_i - b_i(R_{NIR} - Min_{NIR}), \quad (1)$$

Here,

R'_i: the sun-glint corrected pixel brightness in band i;
R_i: the reduced pixel value in band i according to the product of regression slope;
b_i: the regression line slope between band i and the NIR band;

R_{NIR}: the corresponding pixel value in NIR band;
Min_{NIR}: the minimum NIR value existing in the sample.

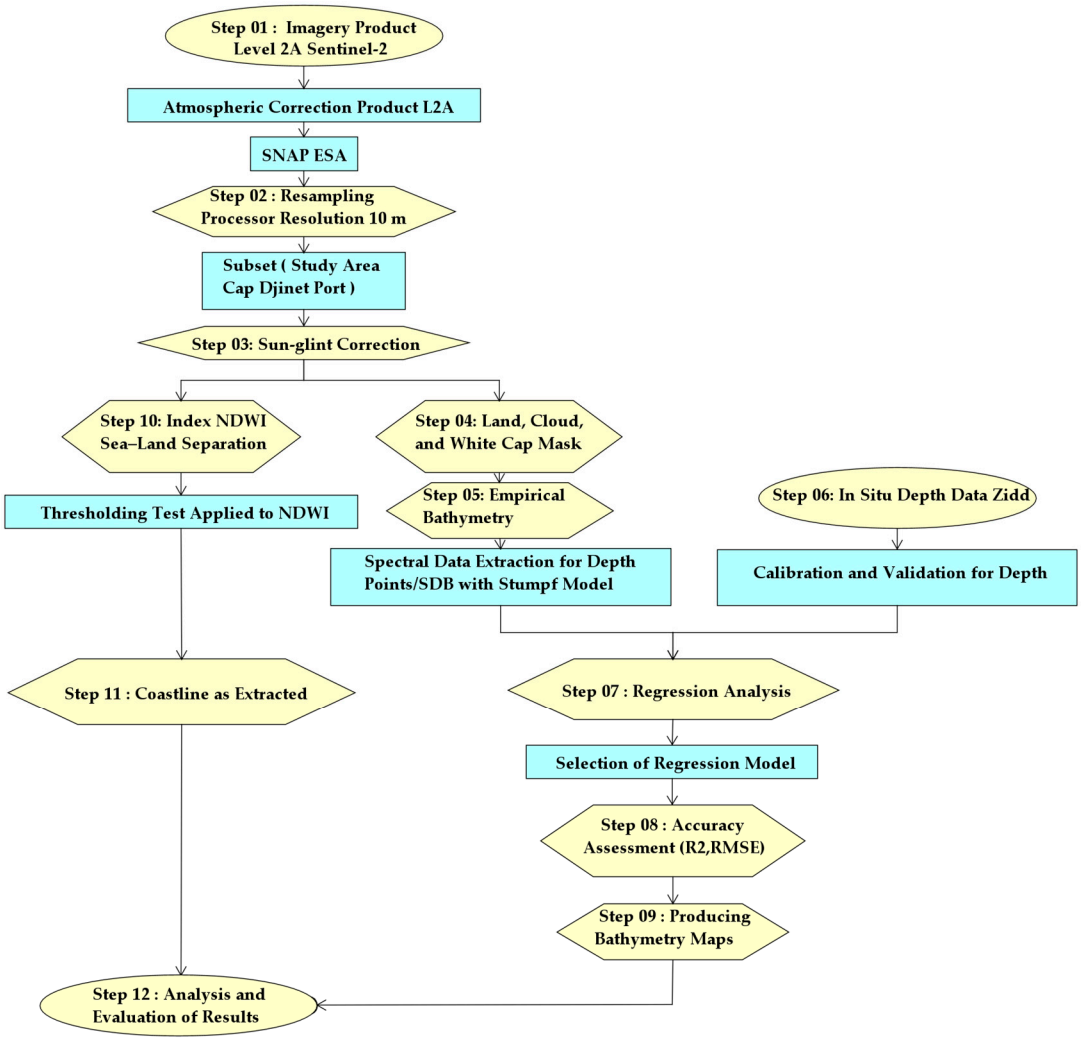

Figure 3. Workflow processing steps for bathymetry detection and coastline evolution from optical images.

Equation (1) was applied to the three visible bands—namely, Band 2 (Blue band), Band 3 (Green band), and Band 4 (Red band)—thus yielding the three sun-glint-corrected bands.

An essential pre-processing step consists of masking the land, white caps (sea foam crest over the waves), clouds, and cloud shadows. The first three masks refer to bright features that can identified due to the fact that the near-infrared wavelengths do not penetrate water; thus, after glint removal, clear areas of water appear very dark. Clouds, white caps, and land typically have high reflectance in the NIR band.

The next step is the empirical bathymetry processor. Estimation of bathymetry via empirical regression is a commonly used method for mapping shallow water areas. However, this method is only applicable if in situ data are available for the area of interest. These most commonly come from a boat sonar system and, in combination with cloudless and calm water images, can be used as an input to the simple regression method and for calibration of the bathymetry retrieval algorithm. It is based on the principle that the water attenuation coefficients differ between wavelengths (bands), such that the ratio between the two bands (which will change with water depth) can be easily determined. In this step, the in situ depths for each point are loaded into a text file, which are then imported into

SNAP as pins, in order to extract the SDB with Stumpf model values from Sentinel-2 data corresponding to each of these points.

The following Equation (2) is used to determine the depth Z_{SDB} in the near-shore coastal area:

$$Z_{SDB} = m_1 \frac{\ln(nR_{rsi})}{\ln(nR_{rsj})} - m_0 \quad (2)$$

where Z_{SDB} is the bathymetry derived from the pre-processed Sentinel-2 image, R_{rsi} and R_{rsj} are the above-water surface remote sensing reflectances of different wavelengths for bands i (blue) and j (green), and m_0 and m_1 are the offset and gain values to linearly transfer the model results to water depths. The values of m_1 and m_0 can be obtained by minimizing the difference between the estimated depth Z and the a priori value of water depth H. Furthermore, n is a fixed constant (which is usually taken as 1000), mainly intended for keeping the log values positive in any condition [34].

The sixth stage concerns the correct distribution of calibration and the validation of the in situ measured water depth Z_{IDD}. The in situ depth data were divided into two packages: one for calibration (80%) and one for validation (20%) [60].

The seventh step consists of regression analysis of the measured water depth "Z_{IDD}" values and "Z_{SDB}" values from the empirical method and the satellite-derived bathymetry (SDB) technique of Stumpf. The relationship between Sentinel-2 satellite data and water depth measurements can be obtained by developing an appropriate regression model. Calibration of the measurement data is necessary to form the linear regression equation.

The eighth step of this methodology consists of studying the performance and evaluating the accuracy of regression model. This performance evaluation measures, in particular, the coefficient of determination (R^2; Equation (3)), which indicates the regression model's "goodness of fit". On the other hand, the adjusted R^2 penalizes the R^2 value for each predictor variable in the regression model (in this case, the input variable).

$$R^2 = \left[\sum_{i=1}^{N} (Z_{IDD} - \overline{Z_{IDD}})(Z_{SDB} - \overline{Z_{SDB}}) / \sum_{i=1}^{N} (Z_{IDD} - \text{mean}(Z_{IDD}))^2 \sum_{i=1}^{N} (Z_{SDB} - \text{mean}(Z_{SDB}))^2 \right] \quad (3)$$

The root-mean-square error (RMSE) can be calculated with Equation (4):

$$RMSE = \sqrt{\frac{1}{N} \sum_{i=1}^{N} (Z_{SDB} - Z_{IDD})^2} \quad (4)$$

where Z_{SDB} is the satellite-derived bathymetry depth, Z_{IDD} is the in situ depth data, and N is the number of water depth measurement points.

The ninth step consists of producing bathymetric maps after validating the Z_{SDB} regression model as a Z_{IDD} function. Next, the tenth step mainly focuses on separation of the land and sea using the NDWI index. This separation technique can only be applied to ports that do not suffer from significant tidal regimes (less than 20/30 cm tidal range amplitude). The latter is only performed after sun-glint correction of the bands using the Sen2coral Algorithm version 9.0.0. The eleventh step consists of extracting the coastline of the study area. This extraction is performed after processing and, in particular, for application of thresholding to the NDWI map, it is suggested to use a mean filter (raster/Filtered Band) on a land/water mask in SNAP, in which everything that is clear land is indicated by a color value of 255, while everything that is clearly water is indicated by a color value of 0. This provides a definition for thresholds (one for the upper and another for the lower) for which values shall be considered as coastline, which can be determined using the Band Maths package. The last step of the methodology consists of analysis and evaluation of the results.

2.5. Ratio Transform Algorithm (Stumpf, 2003)

Satellite-derived bathymetry (SDB) is a useful reconnaissance tool that can be used to map the near-shore bathymetry, characterize coastal areas, and monitor seafloor changes that may have occurred since the last hydrographic survey was conducted. The present study utilizes the application proposed in [34], in which a ratio transform algorithm was developed to determine the bathymetry for shallow waters. The ratio transform algorithm makes use of two bands in order to reduce the number of parameters when determining the near shore bathymetry. The ratio transform algorithm can retrieve depths up to 20 m, and their results showed a good correlation between the algorithm-derived value and the hydrographic chart sounding value [62]. This method is a practical tool for studying near-shore areas before carrying out high-resolution hydrographic studies.

2.6. Normalized Difference Water Index (NDWI)

The objective of this study is to analyze the land–sea separation using the NDWI, which is considered a very effective index for separating land and sea due to the high absorption of electromagnetic radiation by water surfaces, resulting in low radiation reflectance. During the tenth data processing step, a threshold image of the NDWI is created. The water presence index, varying from −1 to +1, was extracted from the satellite imagery in order to locate the coastline. In NDWI, the green wavelength is used to intensify the reflectance of water and the water feature limits the low reflectance of NIR [47]. The NDWI algorithm was applied to bottom-of-atmosphere (BOA) reflectance bands obtained from the SNAP Sen2coral processor version 9.0.0. The NDWI was calculated according to the equation described in Table 4.

Table 4. Details of the water pixel extraction index (NDWI).

Index	Algorithm (Equation)	Threshold Rules for Water Pixels	Author	Area of Study
NDWI	$\frac{Green-NIR}{Green+NIR}$	positive values > 0.0	Mcfeeters; 1996	Clear water; water, soil, and vegetation

3. Results

In order to collect as much information as possible to establish bathymetric maps using the satellite data for our study area—Cap Djinet port—Sentinel-2 products (2A/S2MS-L1C, 2B/S2MSL1C and 2A/S2MS-L2A, 2B/S2MS-L2A) for the period from 9 August 2015 to 28 July 2023 were used after selecting the area of interest and the appropriate search criteria, namely, the visual selection of images without clouds in the date of 31 December 2023 from the link https://browser.dataspace.copernicus.eu. Figure 4 presents circular diagrams of the Sentinel-2 products downloaded for the study area. For the Sentinel-2 2A/L1C product, out of a total of 314 images in the original data set, 48.7% (153) were without cloud cover, 43.0% (135) had cloud cover, and 8.3% (26) were not available. Considering Sentinel-2 2B/L1C, for a total of 236 images, 48.7% (115) were selected without cloud cover, 49.6% (117) had cloud cover, and 1.7% (4) were not available.

For the Sentinel-2 L2A products, these data have been processed with atmospheric corrections in the COPERNICUS/S2 link after the date of 30 April 2017 for 2A/S2MSl, and the date of 21 December 2017 for 2B/S2MSl. Considering Sentinel-2 2A/L2A, a total of 242 images were collected, in which 52.5% (127) were selected without cloud cover, 45.0% (109) had cloud cover, and 2.5% (6) were not available. For Sentinel-2 2B/L2A, of a total of 219 images, 47.0% (103) were selected without cloud cover, 51.1% (112) had cloud cover, and 1.9 % (4) were not available.

The Level-1C orthorectified 2A/2B Sentinel-2 cloud-free images acquired for 30 July 2015 and the two dates of 30 April and 21 December 2017 (37 cloud-free images) were subjected to atmospheric correction using the SEN2COR processor [63]. As we are interested in Sentinel-2 2A/2BLevel-2A products, a database of 317 images without cloud cover from

30 July 2015 to 30 December 2023 was created. These images were transformed into satellite bathymetric survey maps in order to monitor the silting of the port of Cap Djinet.

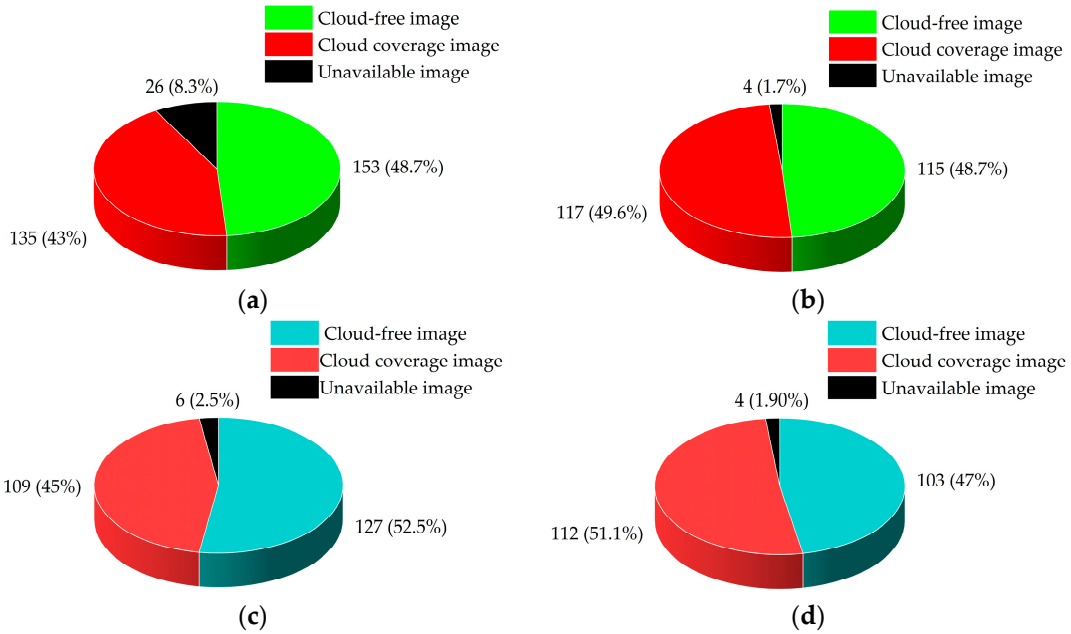

Figure 4. Circular diagrams of Sentinel-2 products for the study area: (**a**) product 2A/S2MS-L1C from 30 July 2015 to 25 December 2023; (**b**) product 2B/S2MS-L1C from 4 July 2017 to 30 December 2023; (**c**) product 2A/S2MS-L2A from 30 April 2017 to 25 December 2023; and (**d**) product 2B/S2MS-L2A from 21 December 2017 to 30 December 2023.

In order to validate the conditions of use and exploitation of our database, a regression analysis was carried out to estimate the correspondence between the data obtained in situ and the satellite bathymetric results for four periods (Figure 5). These images were processed according to the chronology of the methodology previously described (Figure 3), namely, the re-sampling of all of the bands at a 10 m resolution; sun-glint correction using the Sen2coral Algorithm; and land, cloud, and white cap masking. Figure 5 shows the distribution of the calibration points in green color and that of validation points in red color, this distribution having been aligned under the corresponding satellite images.

As satellite sensors refer to a spatial resolution of 10 m, an extrapolation of the points, based on their average value per pixel, was conducted. The coordinates (longitude, latitude) of the depth calibration points, measured in SNAP in the form of pins, allowed us to extract the SDB values (Band2/Band3) corresponding to each of the points. A comparison was developed between the SDB bathymetry points and the in situ measurements at the calibration depth points. The coefficient of determination R^2, the mean absolute error (MAE), and the root-mean-square error (RMSE) were analyzed to determine the generalization capacities of the regression models. These coefficients can be calculated using Equations (3) and (4). The results of the regression analyses for the four dates are shown in Figure 6.

The R^2, MAE, and RMSE values depicted in Figure 6 indicated a satisfactory agreement between the measurements and the calculations with the Stumpf model, except for the January 2021 data (Figure 6b). This led us to think about the factors which influence the satellite bathymetry results. These results are influenced by many uncontrollable environmental factors, reinforcing the uncertainties in the results [60]. The accuracy of bathymetry calculation with passive receivers is affected by water quality (turbidity), cloud cover, weather conditions, and sun glare. Let us consider water quality and weather conditions.

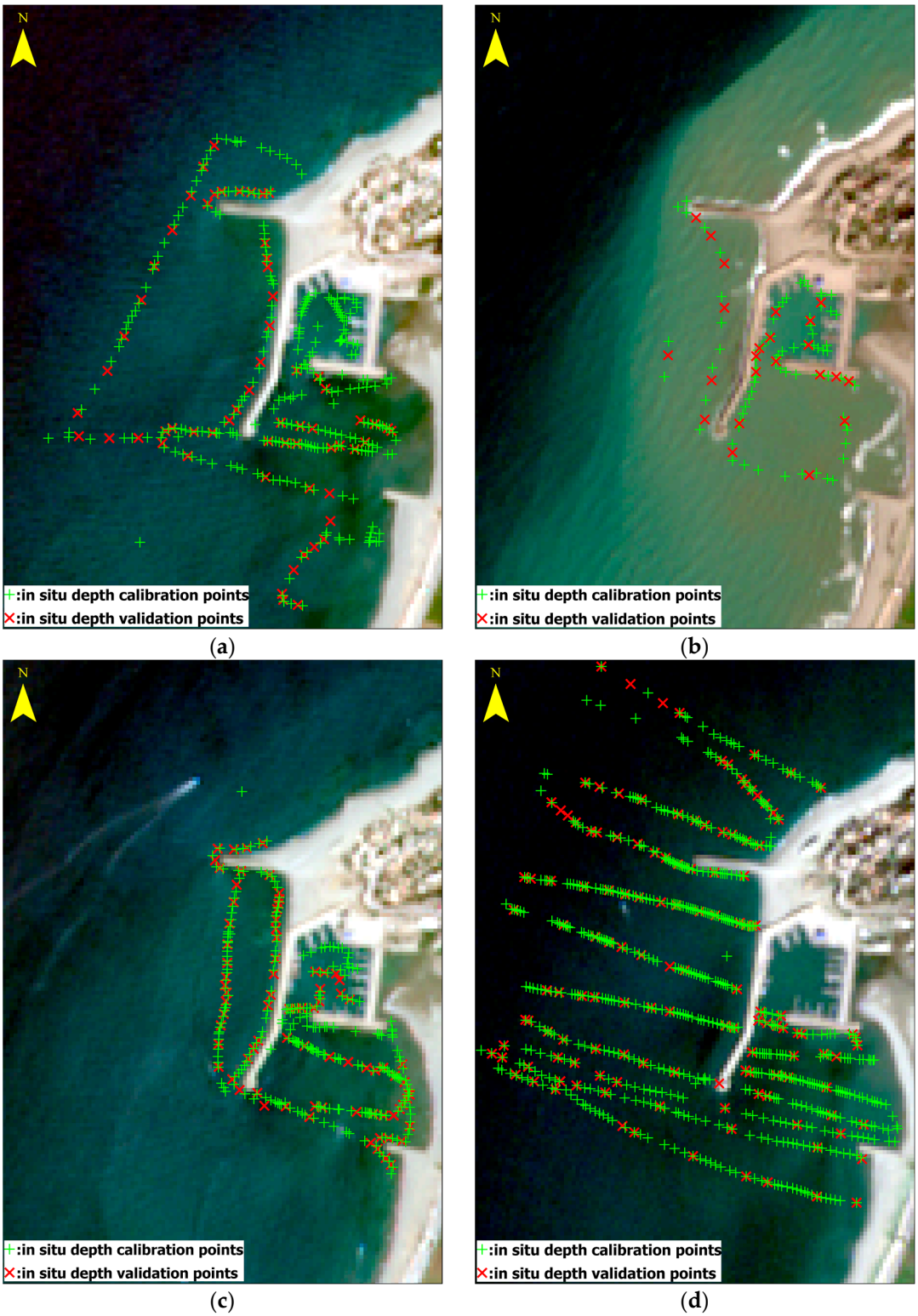

Figure 5. Distribution of in situ depth measurement data points on the Sentinel-2 A and B/L2A satellite maps: (**a**) water depths from 12 August 2020 on the Sentinel-2B/L2A satellite map dated 7 August 2020; (**b**) water depths from 5 January 2021 on the Sentinel-2B/L2A satellite map dated 25 December 2022; (**c**) water depths from 14 August 2022 on the Sentinel-2A/L2A satellite map dated 12 August 2022; and (**d**) water depths from 27 December 2022 on the Sentinel-2B/L2A satellite map dated 25 December 2022.

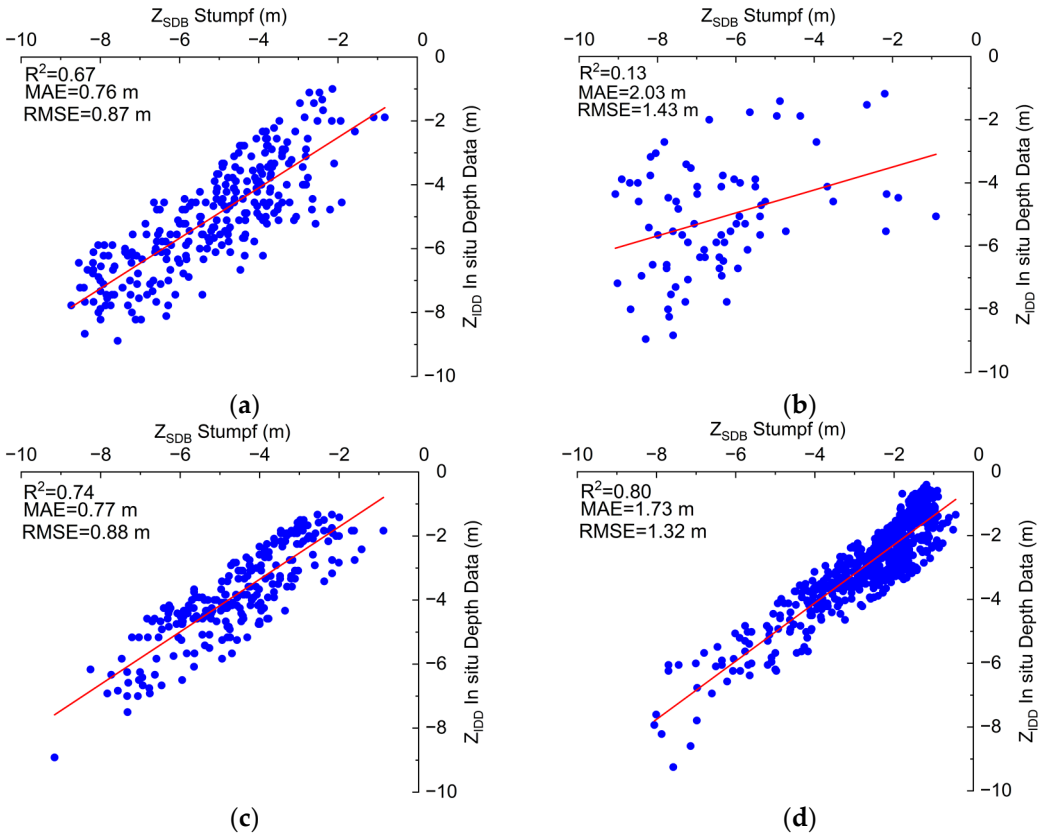

Figure 6. Comparison between SDB bathymetric points obtained with Stumpf (2003) model and in situ depth measurements obtained from calibration points: (**a**) correlation of SDB dated 7 August 2020 and bathymetry surveyed on 12 August 2020; (**b**) correlation of SDB dated 4 January 2021 and bathymetry surveyed on 5 January 2021; (**c**) correlation of SDB dated 12 August 2022 and bathymetry surveyed on 14 August 2022; and (**d**) correlation of SDB dated 25 December 2022 and bathymetry surveyed on 27 December 2022.

Observation of the image from 5 January 2021 (Figure 5b) shows that the water was turbid. The port is located between two large wadis, "Isser" and "Sebaou", making the area highly subject to sediment transport. During rainfall, one or two of the wadis may flood, causing sediment to be discharged and transported into coastal waters. This image was captured after a recorded flood, which happened at the end of December in 2020. The unsatisfactory comparison between the measurements and the calculations with the Strumpf model for this date highlights that satellite SDB bathymetry does not work properly in turbid areas. Turbid waters produce false banks in the imagery, which limits the routine application of SDB [64]. In comparison, the obtained results from very clear images (Figure 5a,c,d) with perfect atmospheric conditions and no flooding before their acquisition were found to be reliable (Figure 6a,c,d). The identification of the best period for bathymetry estimation is, thus, essential.

Concerning the oceanographic conditions, the port of Cap Djinet is not influenced by significant tidal regimes. A significant wave height of combined wind waves and swell data from ERA5 hourly data of ECMWF was used, covering the 2 years between 2020 and 2022 [57]. According to the recording of swell data at the closest point to the port of Cap Djinet (longitude and latitude 37° 7.200′N and 3° 42.000′E), the significant wave heights Hs for the three images depicted in Figure 5a,c, and d were 0.78 m, 0.40 m, and 0 m, respectively; however, a height of Hs = 1.44 m was observed for the image presented in Figure 5b. These results confirm that sea agitation has an influence on the agreement between satellite bathymetry and in situ measurements: the stronger the wave

conditions, the higher the turbidity, and the poorer the agreement between the results derived from satellite imagery and in situ measurements.

Table 5 presents the linear regression equations between the Stumpf SDB Bathymetry and depth data from in situ calibration points for August 2020, August 2022, and December 2022.

Table 5. Linear regression equations of Z_{SDB} Stumpf and depth data from in situ calibration points.

Measurement Campaign Number	Algorithm	Date of Acquisition by Satellite	Dates for In Situ Depth Calibration Points	Best Fit for Depth Estimation between Satellite and In Situ Measurements
1	Ratio Transform Algorithm Stumpf	7 August 2020	12 August 2020	y = 5.71 + 2.19x
3		12 August 2022	14 August 2022	y = 9.86 + 3.58x
4		25 December 2022	27 December 2022	y = 1.17 + 1.15x

In order to validate the above equation models, an implementation of the longitude and latitude coordinates of the validation points in SNAP, in the form of pins, was carried out. This allowed us to extract the SDB values corresponding to each validation points. According to the linear equations shown in Table 5, the Stumpf Z_{SDB} water depth (y) was calculated based on the extracted SDB values. A comparison was established between the reserved validation points and the Z_{SDB} calculated water depths. The coefficient of determination (R^2), mean absolute error (MAE), and root-mean-squared error (RMSE) values were analyzed to determine the generalization capacities of the proposed correlations. The results of the regression analyses for the three periods of the measurement campaigns are represented in Figure 7.

The results show high R^2 coefficient values and lower values of the MAE and RMSE coefficients for the in situ depth measurements than for the calibration points (Figure 6). The observed and estimated values were well-correlated when using the validation points for the in situ measurements (Figure 7).

The application of the Stumpf Algorithm on the satellite images captured between 2015 and 2023, bearing in mind the conditions of use, allowed us to obtain bathymetric surveys according to the different periods selected. The determination of the seabed evolution for the considered profiles and period, as described in the work of the authors of [65], enabled us to estimate the accretion and erosion zones, as well as their volumes and heights.

Concerning the study of the evolution of the coastline in the vicinity of the port using the NDWI for the separation of the water body from the land, a distance of 2.25 km to the north and south of the port was considered. This study was based on a period of 8 years, where approximately 317 cloud-free images were selected, with the images filtered for the summer season (month of August), during which the water is generally clear, as the presence of turbidity in a satellite image reduces the efficiency of indices used for delineating water bodies [66].

Figure 8 shows the shoreline extraction results for the images acquired from 2015 to 2023. The application of the NDWI on the original images allowed for good separation between the sea and the land with a spatial resolution of 10 m, with values of this index greater than 0 for the sea surface and less than 0 for the land surface vegetation and soil [46]. This confirms that near-infrared wavelengths are strongly absorbed by the water mass and reflected by dry soils and vegetation [67]. The coastline was extracted on the basis of the images of the NDWI through determining its optimal threshold value, with negative pixel values being replaced by the value 0, and varying the positive pixel values from 0 until observation of the coastline configuration (optimal threshold). After this observation, the coastline was marked using a tool in the SNAP Pin Manager, which located each pixel corresponding to the coastline observed in the processed image and transformed it into (x, y) coordinates for georeferencing in Arcgis Pro 3.1.0.

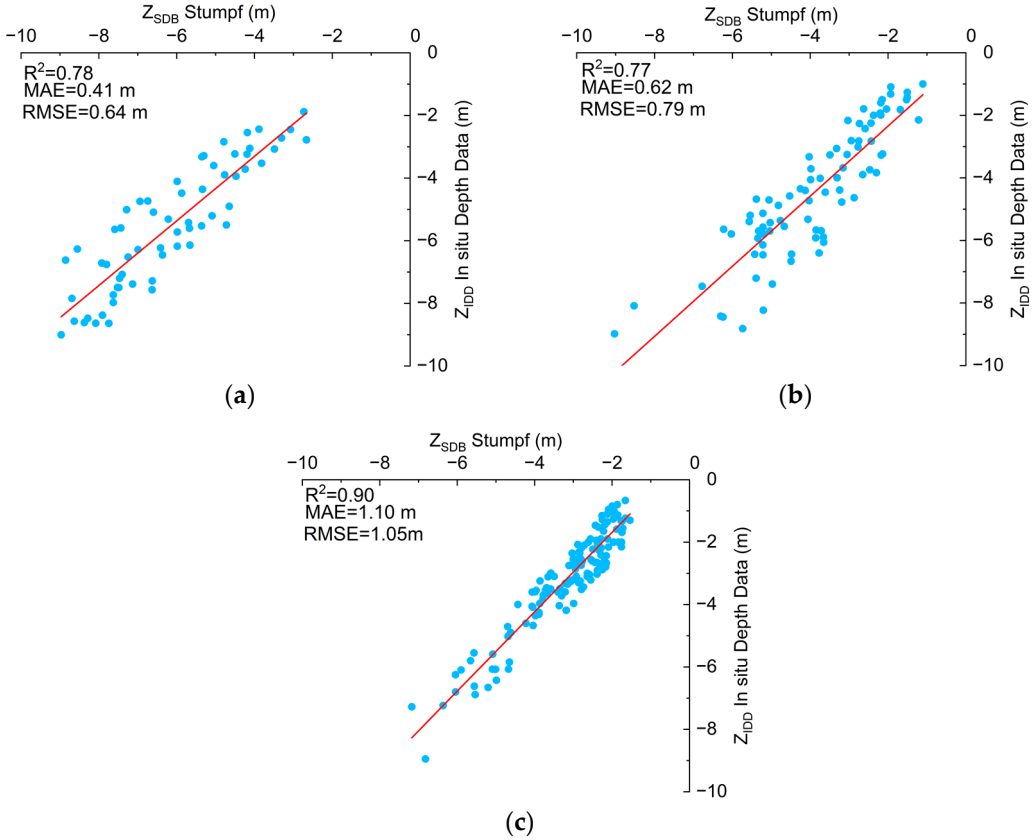

Figure 7. Comparison between SDB bathymetric points obtained with Stumpf (2003) model and in situ depth measurements obtained from in situ validation points: (**a**) correlation of SDB dated 7 August 2020 and bathymetry surveyed on 12 August 2020; (**b**) correlation of SDB dated 12 August 2022 and bathymetry surveyed on 14 August 2022; and (**c**) correlation of SDB dated 25 December 2022 and bathymetry surveyed on 27 December 2022.

Through superimposing the two bathymetric surveys extracted from each satellite image (with different recording dates), we could detect and quantify the volumes of deposition and erosion in terms of altimetry, using long profiles drawn up from the shore to the open sea and covering various locations in the study area.

In order to appreciate the results obtained according to the NDWI, Figure 9 represents the frequency density histograms as a function of the NDWI. This figure shows clear distributions with significant peaks for water and land. These peaks are more dissociated than in the case of [68], indicating better differentiation between the two substrates.

The presented method using threshold values was found to provide a very good delimitation of the coastline with great precision in the vicinity of the port of Cap Djinet, which makes it possible to carry out interannual monitoring of accretion and erosion zones. For this purpose, the coastlines extracted every two years from 2015 to 2023 were superimposed. Figure 10 presents the location of the erosion and accretion zones, with indication of the corresponding surfaces as well as their percentages. It can be deduced that the port of Cap Djinet has undergone morphological and hydrographic variations, showing progressive sediment accumulation in the southeast part of the port between the secondary jetty and the southern groyne, which indicates the significant transit of sediments leading to a sedimentary imbalance in this area.

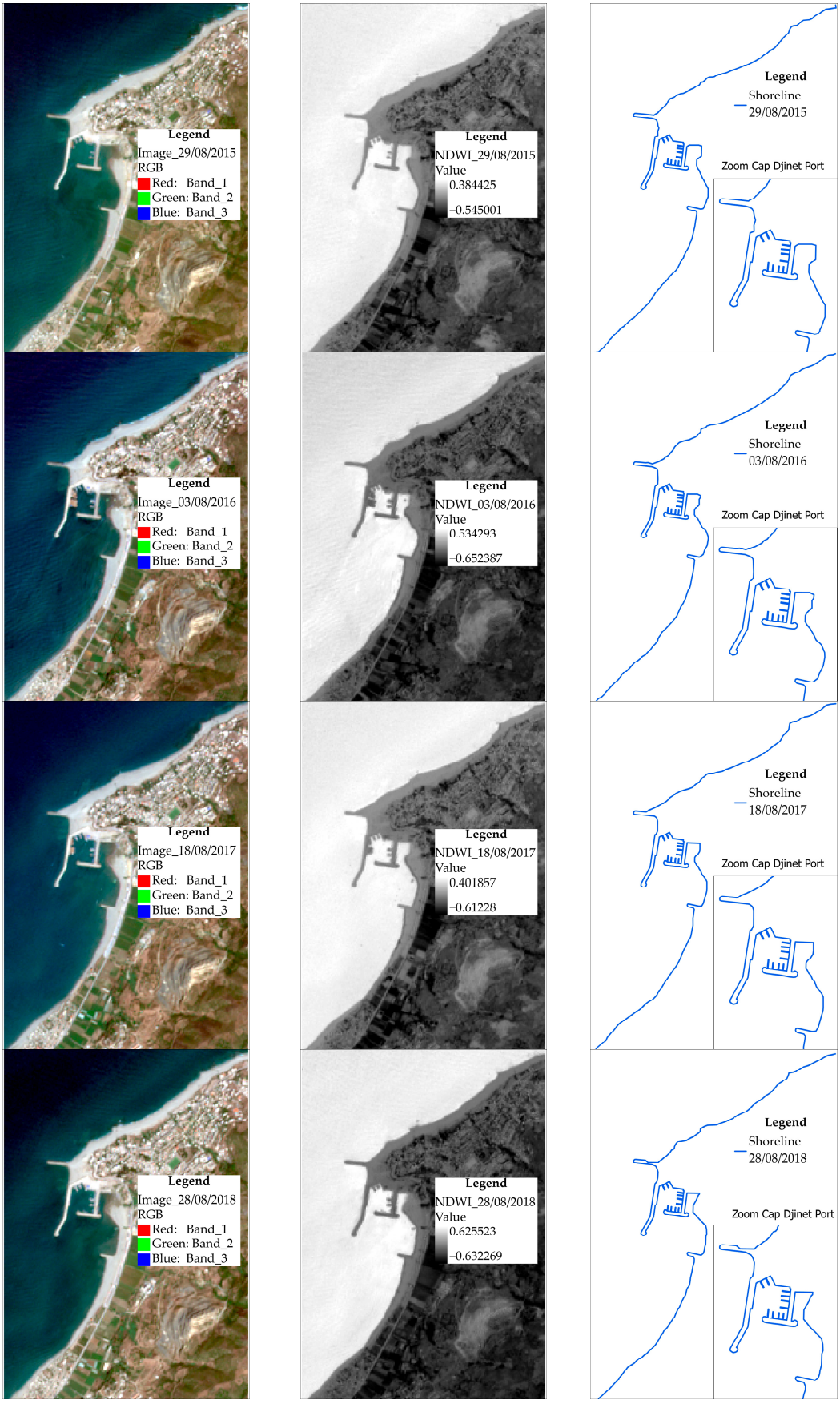

Figure 8. *Cont.*

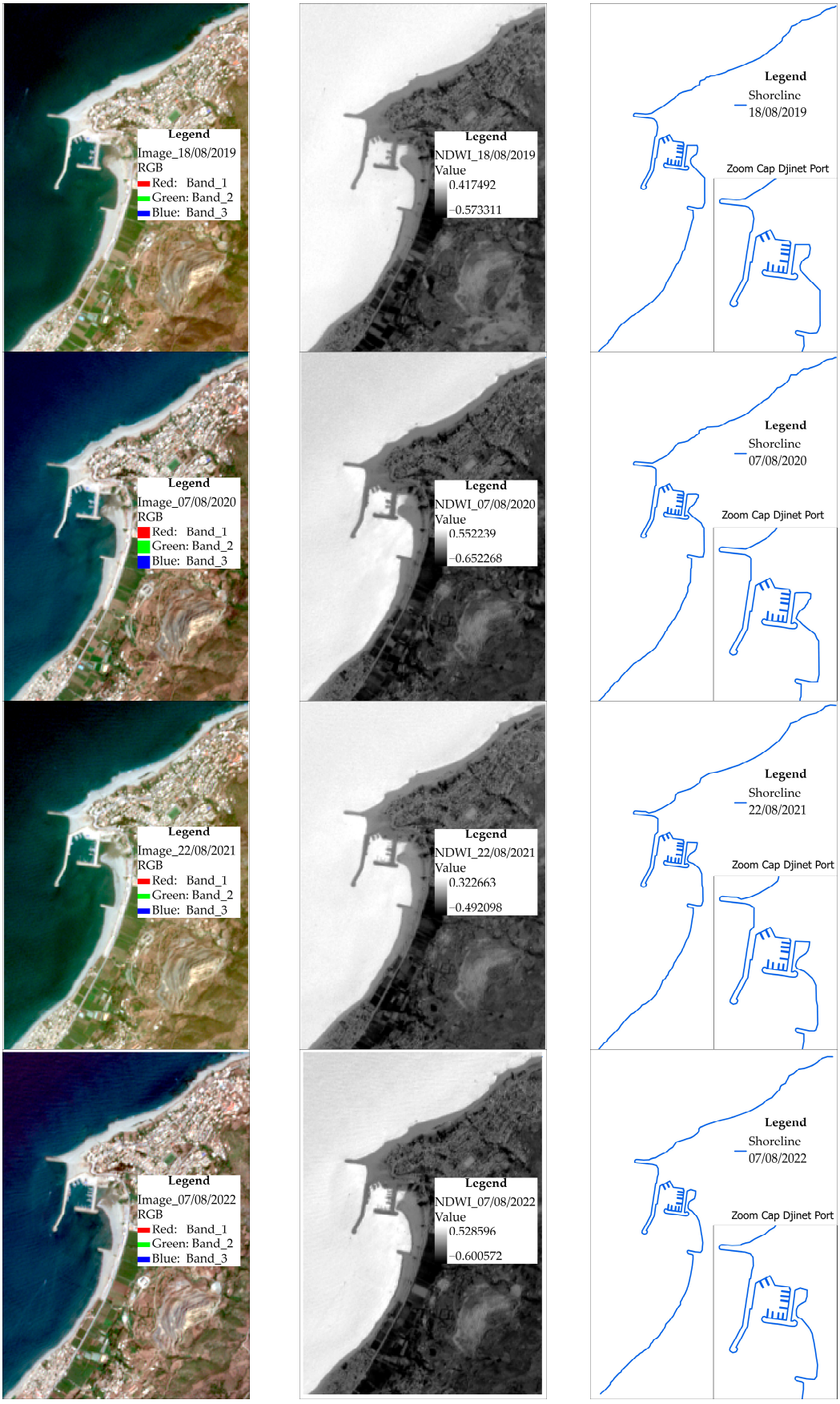

Figure 8. *Cont.*

Figure 8. Shoreline extraction for images acquired from 2015 to 2023: (**a**) original images; (**b**) normalized difference water index (NDWI) applied to the original images; and (**c**) coastline extracted.

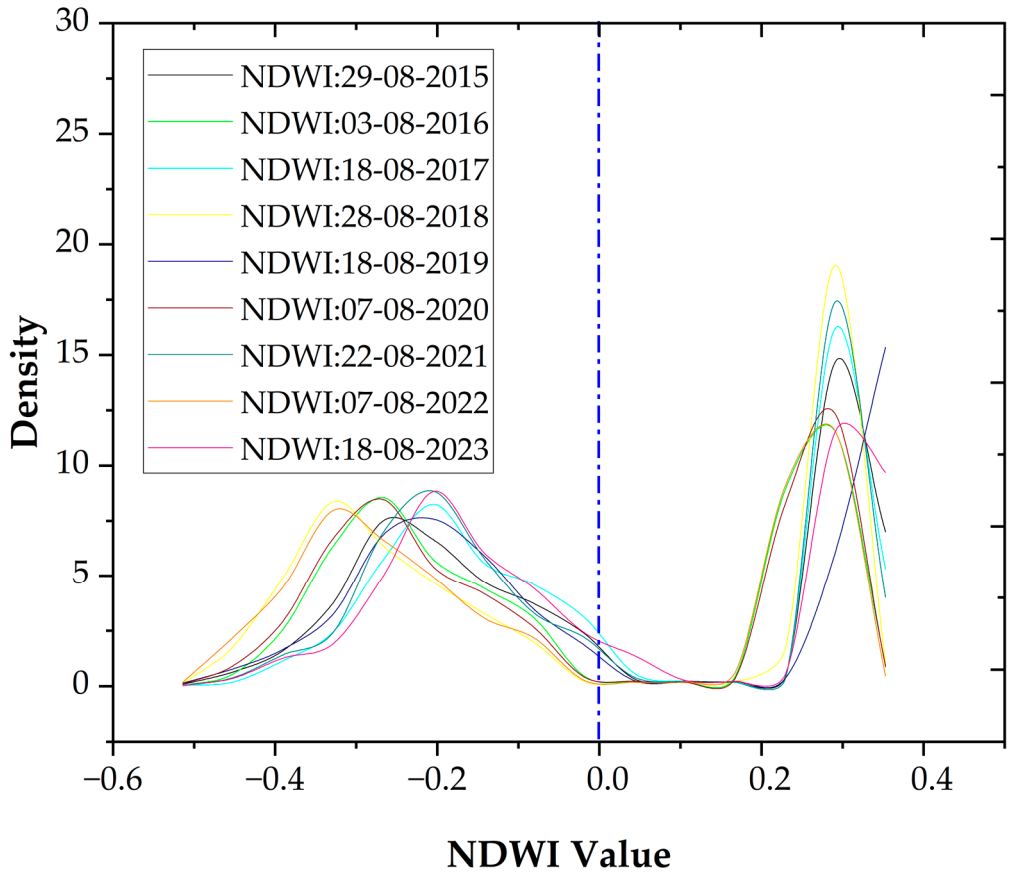

Figure 9. Density distributions of the NDWI. The vertical dotted blue line indicates the threshold value T $\geq$ 0.00.

The areas of erosion and accretion in the north and south of the port between 2015 and 2023 are detailed in Table 6.

According to the analysis of the figures cited above, a maximum value of uncertainty of the accretion surface of 2.82 Ha was observed between 2015 and 2016, and a maximum value for the uncertainty of the erosion surface of 1.35 Ha was observed between 2017 and 2018. Figure 11 separately depicts these surfaces to the north and south of the port.

Table 6. Total areas of accretion and erosion in the studied area.

	Total Areas	
Year	**Accretion Area (Ha)**	**Erosion Area (Ha)**
2015–2016	3.41	0.59
2016–2017	1.51	1.93
2017–2018	2.19	3.54
2018–2019	3.59	1.45
2019–2020	1.54	2.05
2020–2021	2.44	1.37
2021–2022	1.13	1.57
2022–2023	1.03	1.22
Total	16.83	13.72

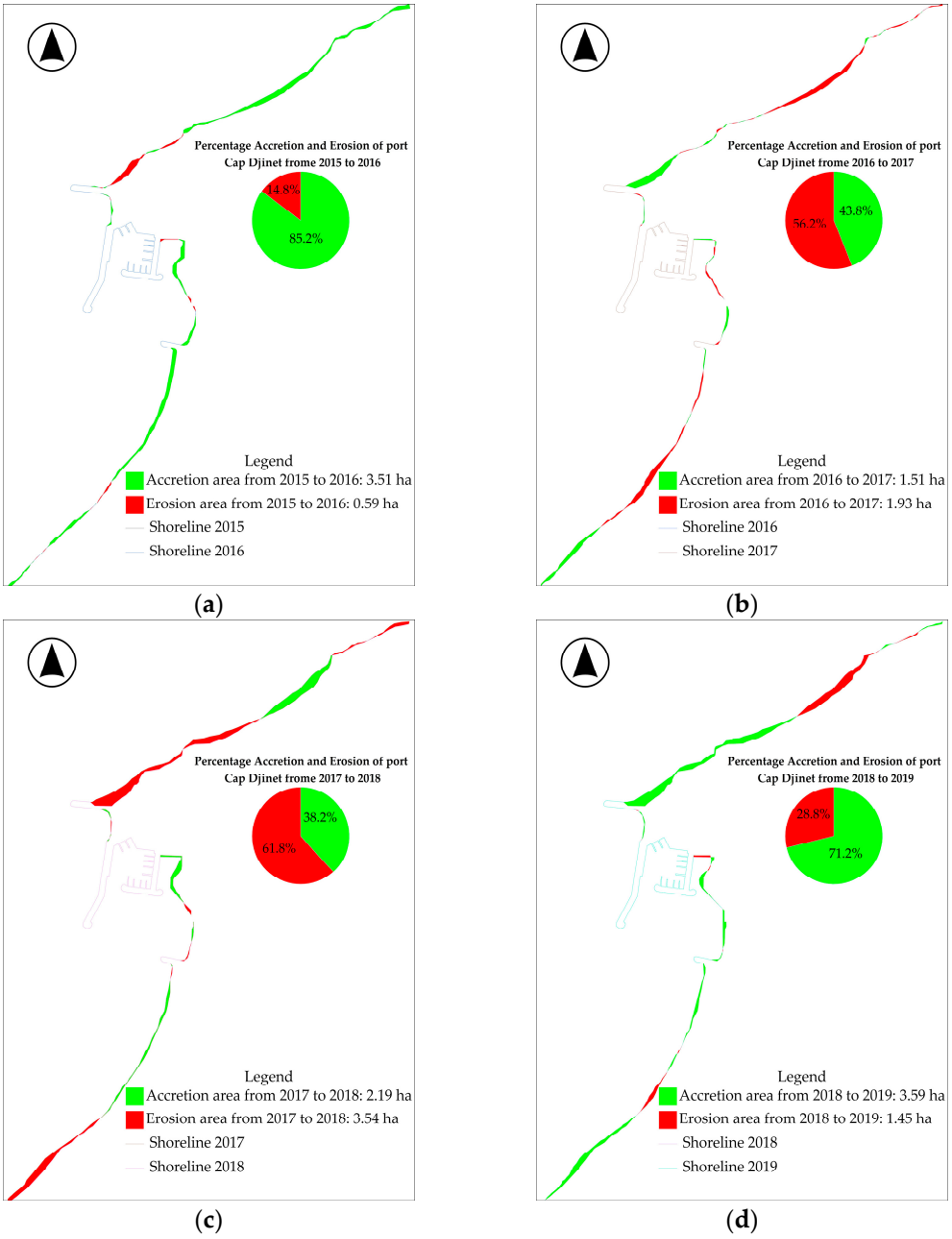

Figure 10. *Cont.*

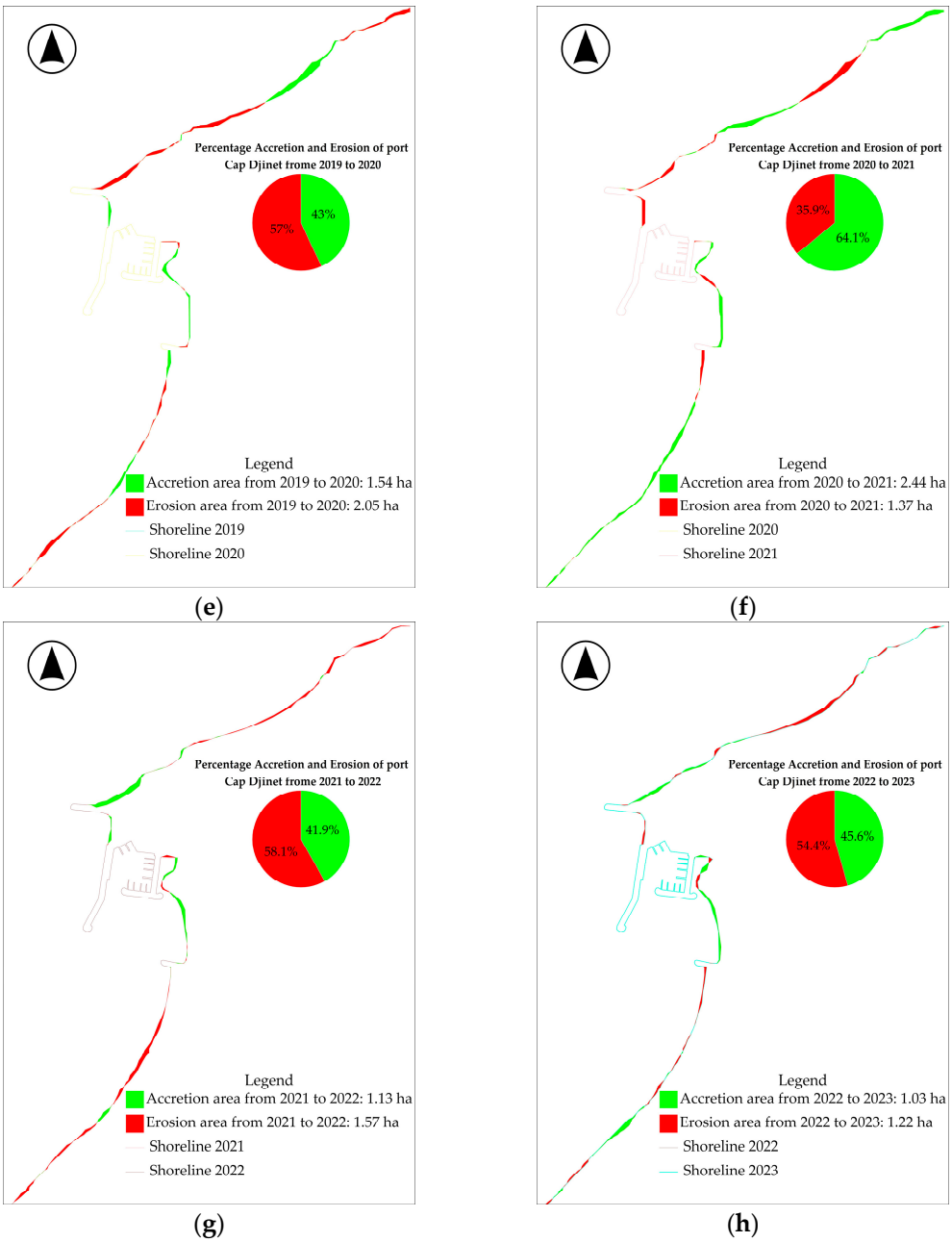

Figure 10. The location of the erosion and accretion zones near the port of Cap Djinet: (**a**) accetion and erosion from 2015 to 2016; (**b**) accetion and erosion from 2016 to 2017; (**c**) accetion and erosion from 2017 to 2018; (**d**) accetion and erosion from 2018 to 2019; (**e**) accetion and erosion from 2019 to 2020; (**f**) accetion and erosion from 2020 to 2021; (**g**) accetion and erosion from 2021 to 2022; (**h**) and accetion and erosion from 2022 to 2023.

A maximum deposit area of 2.12 ha to the north of the port was observed between 2018 and 2019, while the maximum deposit area was 1.78 ha to the south of the port for the period 2015–2016. The coastline advanced by 50.0 m per year to the north (Figure 8) and by a maximum of 20.0 m per year to the south (Figure 8a). As a result, sedimentation developed mainly north of the north groyne. On the other hand, a maximum erosion area of 2.37 ha was reached to the north of the port between 2017 and 2018, while a maximum area of 1.16 ha occurred to the south of the port between 2017 and 2018. The coastline receded by 57.0 m per year to the north, and by a maximum of 31.0 m per year to the south (Figure 8c). The cumulative deposit area to the north of the port was 8.80 ha, greater than

that (8.03 ha) to the south of the port. Additionally, the cumulative erosion surface to the north of the port was 8.79 ha, much greater than that (4.93 ha) to the south of the port. These results indicate that larger areas to the north of the port are subject to accretion or erosion when compared to the south. Following the result of the numerical model developed by the authors of [69], northern directions are the most frequent and energetic. Changes resulting in accretion and erosion surfaces in the north and the south are generally caused by past strong storms in the considered area.

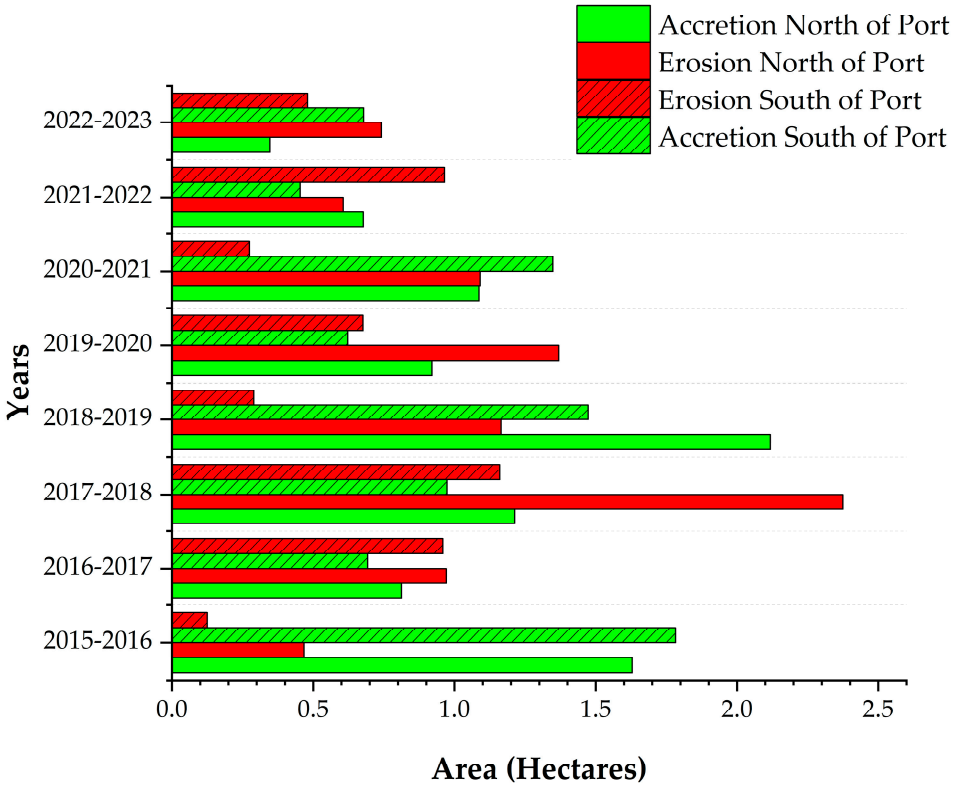

Figure 11. Areas of accretion and erosion north and south of port Cap Djinet.

During storms, the waves push the sediment on both sides (i.e., north–south and south–north) due to coastal transport, resulting in a change in the shoreline morphology, with significant accretion occurring in the convergence zone.

Nevertheless, the south beach is also subject to sand accumulations, originating from both the north and south sectors due to the offshore wave regime. Sands trapped by the north and south groynes exhibit different granulometric characteristics; coarse sand is predominant at the north beach, while fine muddy sand prevails at the south beach. However, sediment samples collected in the south sector during the experimental phase at sea revealed a mixture of gravel (22%), sands (40%), and silt (38%) in the south surf zone. This finding could potentially explain the sediment dynamics in this area and support the hypothesis of sand transfer from the north to the south during periods dominated by north storm episodes [70]. As a result, sediments are easily transported by currents to the south of the port, justifying the strong hydrodynamics to the north resulting in areas of accretion and erosion. Returning to the storm history in this area, considering the strong storm on March 6th 2009, the port was declared completely silted up after this storm, with an accumulation of sand along the main jetty and widening of the beach to the northeast of the port. This phenomenon of silting was accentuated, resulting in the creation of a sand spit arrow in the shelter of the north part of the main jetty. Subsequently, smaller storms induced the same problem. There was still a significant accumulation of sand on the northern groyne on the 15 and 16th of May in 2011 and the 24th of January in 2012. This confirms the major sediment displacements in the north part of the port. It is necessary

to carry out in-depth research on the effects of storms on the silting of port of Cap Djinet, considering significant wave heights, wave directions, and storm durations.

As mentioned in Section 2.1, this coastal area of the province of Boumerdes is furrowed by two important wadis: Wadi Isser located at an approximate distance of 6.0 km southwest of the port of cap Djinet and Wadi Sebaou located about 13 km northeast of the port. Wadi Isser has a catchment area of 3615 km^2, and the annual solid inputs between 1954 and 1978 have been estimated at 6332.44 million tons, according to the LEM 2009. Wadi Sebaou has a watershed of 2890 km^2. After exceptional floods, a significant amount of sediment coming out of these two wadis converges towards the port of Cap Djinet, according to the LEM 2012 [71]. The location of this port between these two wadis explains the importance of the silting phenomenon in this port. Let us consider the sediment plume at the mouth of these two wadis during a flood, using Sentinel 2/L1C and the SNAP Case 2 Regional Coast Color (C2RCC) processor to extract the TSM (Total Suspended Matter) concentration values [72]. Sentinel 2 and C2RCC data are productive tools for TSM extraction [73]. Figure 12 shows the sediment dispersion after the flood of 24 February 2018.

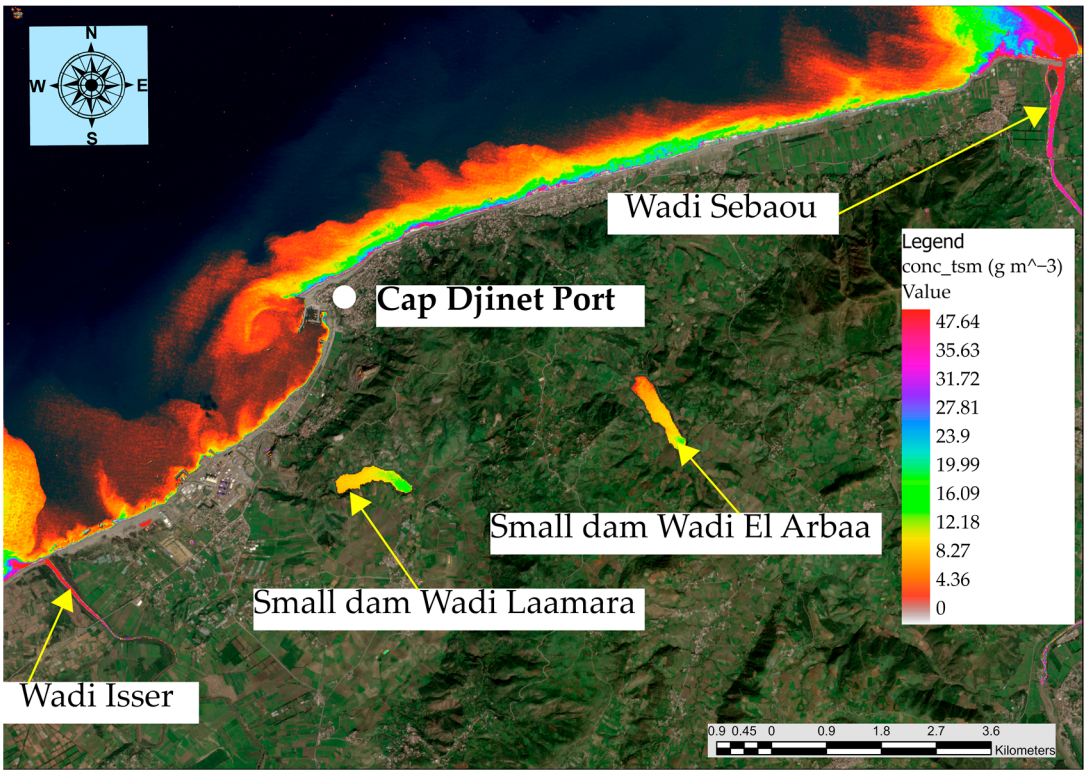

Figure 12. Concentration of TSM (Total Suspended Matter) after the flood of 24 February 2018 around the study area.

This figure confirms the impact of sediments from the two main wadis on the port of Cap Djinet. Regarding sediments from Wadi Sebaou, both waves and tidal drift currents induce sediment transport along the coast, directed towards the northern part and the entrance face of the port [69,70]. According to the results of the latter study on the evolution of fluorescent clouds over time, depth transport was observed at the north beach, with a reshuffle depth exceeding 40 cm, and surface transport at the south beach, where the reshuffle depth did not exceed 10 cm. The detection of red grains in the southern sector confirms the north–south littoral drift direction under the influence of the northeast waves. This aligns with the results of satellite imagery of the northern part, which experiences more sedimentary movement. Meanwhile, sediments from Wadi Isser are transported directly to the south of the port and its entrance face.

4. Discussion

The study area of the Cap Djinet port is characterized by strong sediment transport, leading to a significant change in the morphology of the sea bed in shallow waters. This evolution has been influenced by the spatial variability of the sediments. However, the hydrodynamic and anthropic factors which contribute to the sediment transport could cause disturbances in the hydro-sediment regime of the Cap Djinet port [74]. The Zemmouri bay of Boumerdes may be exposed to very energetic waves, inducing modifications of the sediment transport and of the shoreline [75]. An assessment of the convergence of sediment transport to the Cap Djinet port under different wave regimes has been carried out, based on fluorescent tracer monitoring [70].

Comparison of the bathymetric variation between August 2008 and August 2009 indicated very significant accretion with a balance of 193,462 m^3, which is equivalent to an average sand thickness of 20 cm, with the maximum accumulation value (more than 5 m thick) recorded at the port entrance pass. The port was declared out of service in 2009 [76].

At the beginning of 2011, modification of the development plan was performed by adding a groyne to the north (280 m). During the construction works, a significant accumulation of sand was noted in its upper part, presenting a rating height of 2.85 m following the storms recorded from May 15 to 16 of 2011. The same problem was noted after the storm of January 6 in 2012. In 2014, all of the suggested modifications were implemented, with two groynes built to the north and south, while the main jetty was extended over a length of 150 m with an inclination of 20° relative to the axis from the main jetty (Figure 1). In 2016, two years after these changes of the development plan, the problem still persisted.

The evolution of the coastline clearly shows that the sedimentation levels have increased, particularly in the northern and southern parts. The coastline images extracted from satellite imagery (Figure 1) allowed us to conclude that the modifications performed in 2011 and 2014 did not resolve the problem, and that the sedimentation phenomenon still continued. Dredging has become an emergency solution for the operation and maintenance of this port. A major dredging operation was launched between 2014 and 2018, with the volume of dredged sand during this operation being approximately 100,000 m^3 (i.e., a volume of 25,000 m^3 per year).

The construction of the Cap Djinet port brought sediment rearrangements and modifications to the coastal balance. This port has become a barrier to sediment and, so, sedimentation took place. Sentinel-2 satellite images are very useful for monitoring silting and the coastline morphology, which allows for regular dredging operations of the port and its surroundings, as well as the proposal of effective measures for the future fight against this silting phenomenon. A possibility in the context of this fight is the realization of an adjustment through the creation of the two parallel groynes at the mouth of the wadis, in order to limit sediment transport towards the port and to disperse these sediments towards the sea.

The location of erosion zones using satellite images enables the proposal of an action plan for the future use of sand from dredging operations and for beach nourishment. This may allow sediment balance to be ensured.

The present study, being 8 years in duration, is relatively short given the importance of this subject and the complexity of this area. The Sentinel-2 data have been available since 2015. It is necessary to do further research combining Sentinel-2 and Landsat data in order to cover periods before 2015 [77]. For example, the process of sand spit formation in the shelter of the main jetty according to google image in March 2009 may be analyzed using Landsat data.

The vulnerability of this area is expected to increase in the future due to the effects of the mega desalination station under construction in the southwest of Port Cap Djinet, with an expected production of 300,000 m^3/day. The installation of the water intake pipe with a diameter of 2 × 1500 mm and the development project of the two groynes to protect the desalination plant from silting up will induce additional problems relating

to sediment transport, which should be studied through in-depth research. Other effects of climate change must also be considered, namely, the variation in sea levels, strong storms, and exceptional flooding of wadis. The combination of Sentinel-2 data, in situ measurements, and physical and numerical modelling will provide valuable information for decision making, as well as for the management and monitoring of coastal areas, which could help address the effects of climate change and human activities for the protection of marine ecosystems.

5. Conclusions

The selection of sites for small ports was based solely on numerical models of sediment transport, and small ports along the Algerian coast now must be dredged practically every year. This study aimed to develop a methodology for monitoring the coastline and bathymetry of a small port affected by siltation, combining Sentinel-2 satellite imagery with in situ echosounder measurements. To estimate the bathymetry, the Stumpf logarithmic ratio model was applied to Sentinel-2 images. Regression between the bathymetric echosounder and bathymetric surveys estimated from satellite images yielded high coefficients of determination in the case of favorable oceanographic conditions, in terms of agitation and water quality. The results were as follows under the respective conditions: R^2 = 0.80, MAE = 1.73 m, RMSE = 1.32 m; R^2 = 0.74, MAE = 0.77 m, RMSE = 0.88 m; and R^2 = 0.67, MAE = 0.76 m, RMSE = 0.87 m. However, the regression analysis was inconsistent and presented a poor correlation in unfavorable oceanographic conditions characterized by the presence of turbid water with sea agitation, with correlation parameters as follows: R^2 = 0.13, MAE = 2.03 m, RMSE = 1.43 m. These results indicate that water quality plays an essential role in depth estimation when using the Stumpf model algorithm. The location and estimation of erosion and deposition surfaces were obtained between 2015 and 2023 from the coastlines extracted using the normalized difference water index (NDWI). Areas of maximum accretion were estimated to the north and south of the port: 2.12 ha between 2018 and 2019, and 1.78 ha between 2015 and 2016, respectively. Concerning erosion, a maximum area of 2.37 ha was obtained to the north of the port between 2017 and 2018, while the corresponding area to the south of the port was 1.16 ha between 2017 and 2018. There is a clear separation of sediment deposit areas between the north and south of the port, with major sediment displacements occurring in the north part of the port. Given the complexity of this area, it is necessary to study historical sediment movement data prior to 2015. In the future, we intend to use Landsat images to analyze the characteristics of coastline evolution over a longer period, in order to better understand the mechanism driving coastline evolution in this area. This study confirmed the possibility of using Sentinel-2 satellite data to monitor silting and changes in the coastline near the port of Cap Djinet. Given the complexity of this site, it is necessary to carry out further research taking into account the sediment movements before 2015, that is, the date from which Sentinel-2 data are available. This can be achieved using Landsat images, allowing the evolution of the considered coastline to be analyzed over a long period of time. In order to avoid numerous problems such as those encountered in the port of Cap Djinet, a suggestion can be pointed out: when choosing a site for a small port, consider the combined use of remote sensing, in situ measurements, and physical and numerical modelling, taking into account any flooding that may occur in watercourses in the vicinity of the considered site. This could help to better address the effects of climate change and human activities in order to more effectively protect marine ecosystems.

Author Contributions: Conceptualization, H.D.; Methodology, H.D.; Software, H.D.; Validation, H.D.; Formal analysis, H.D.; Resources, F.H.B.; Data curation, F.H.B.; Writing—original draft, F.H.B.; Writing—review & editing, F.H.B.; Visualization, F.M.; Supervision, F.M. and N.I.B.; Project administration, N.I.B. All authors have read and agreed to the published version of the manuscript.

Funding: This research received no external funding.

Data Availability Statement: Data are contained within the article; further inquiries can be directed to the corresponding author.

Acknowledgments: The authors would like to thank the anonymous reviewers and the editor for their constructive comments and suggestions for this paper.

Conflicts of Interest: The authors declare no conflicts of interest.

References

1. Van Rijn, L.C. Harbour Siltation and Control Measures. Available online: http://www.leovanrijn-sediment.com/papers/Harboursiltation2012.pdf (accessed on 15 March 2020).
2. De Graauw, A. Ancient Port Structures. Parallels between the Ancient and the Modern. *Méditerranée. Rev. Géographique Des Pays Méditerranéens/J. Mediterr. Geogr.* 2022. [CrossRef]
3. Wright, L.D.; Boon, J.D.; Kim, S.C.; List, J.H. Modes of Cross-Shore Sediment Transport on the Shoreface of the Middle Atlantic Bight. *Mar. Geol.* **1991**, *96*, 19–51. [CrossRef]
4. Soulsby, R. *Dynamics of Marine Sands*; Thomas Telford: London, UK, 1997.
5. Winterwerp, J.C. Reducing Harbor Siltation. I: Methodology. *J. Waterw. Port Coast. Ocean Eng.* **2005**, *131*, 258–266. [CrossRef]
6. Cáceres, R.A.; Zyserman, J.A.; Perillo, G.M. Analysis of Sedimentation Problems at the Entrance to Mar Del Plata Harbor. *J. Coast. Res.* **2016**, *32*, 301–314.
7. Niu, J.; Xu, J.; Li, G.; Dong, P.; Shi, J.; Qiao, L. Swell-Dominated Sediment Re-Suspension in a Silty Coastal Seabed. *Estuar. Coast. Shelf Sci.* **2020**, *242*, 106845. [CrossRef]
8. Green, M.O.; Coco, G. Review of Wave-Driven Sediment Resuspension and Transport in Estuaries: Wave-Driven Sediment Transport. *Rev. Geophys.* **2014**, *52*, 77–117. [CrossRef]
9. Boufeniza, R.L.; Alsahli, M.M.; Bachari, N.I.; Bachari, F.H. Spatio-Temporal Quantification and Distribution of Diatoms and Dinoflagellates Associated with Algal Blooms and Human Activities in Algiers Bay (Algeria) Using Landsat-8 Satellite Imagery. *Reg. Stud. Mar. Sci.* **2020**, *36*, 101311. [CrossRef]
10. Caballero, I.; Chapela-Bernatche, L.; Roque-Atienza, D.; Tejedor Álvarez, M.B.; Gomez-Pina, G.; Muñoz Pérez, J.J. *Influencia Del Oleaje En Las Condiciones de Cierre de La Desembocadura Del Río Guadiaro (Cádiz)*; IX Jornadas Españolas de Ingenieria de Costas y Puertos: Cadiz, Spain, 2008; pp. 32–39.
11. Diez, J.J.; Fernando, R.; Veiga, E.M. Coastal Impacts Around Guadiaro River Mouth (Spain). In *Engineering Geology for Society and Territory*; Lollino, G., Manconi, A., Locat, J., Huang, Y., Canals Artigas, M., Eds.; Springer International Publishing: Cham, Switzerland, 2014; Volume 4, pp. 187–190, ISBN 978-3-319-08659-0.
12. Roca, M.; Navarro, G.; García-Sanabria, J.; Caballero, I. Monitoring Sand Spit Variability Using Sentinel-2 and Google Earth Engine in a Mediterranean Estuary. *Remote Sens.* **2022**, *14*, 2345. [CrossRef]
13. Wuthrich, D. *Google Earth Pro*; Geospatial Solutions: Cleveland, OH, USA, 2006; Volume 16.
14. Tonyes, S.G.; Wasson, R.J.; Munksgaard, N.C.; Evans, K.G.; Brinkman, R.; Williams, D.K. Sand Dynamics as a Tool for Coastal Erosion Management: A Case Study in Darwin Harbour, Northern Territory, Australia. *Procedia Eng.* **2015**, *125*, 220–228. [CrossRef]
15. Aleksandrov, S.V. Biological Production and Eutrophication of Baltic Sea Estuarine Ecosystems: The Curonian and Vistula Lagoons. *Mar. Pollut. Bull.* **2010**, *61*, 205–210. [CrossRef]
16. Li, P.; Ren, P. Partial Randomness Hashing for Large-Scale Remote Sensing Image Retrieval. *IEEE Geosci. Remote Sens. Lett.* **2017**, *14*, 464–468. [CrossRef]
17. Nasiha, H.J.; Shanmugam, P.; Sundaravadivelu, R. Estimation of Sediment Settling Velocity in Estuarine and Coastal Waters Using Optical Remote Sensing Data. *Adv. Space Res.* **2019**, *63*, 3473–3488. [CrossRef]
18. Valderrama-Landeros, L.; Flores-de-Santiago, F. Assessing Coastal Erosion and Accretion Trends along Two Contrasting Subtropical Rivers Based on Remote Sensing Data. *Ocean Coast. Manag.* **2019**, *169*, 58–67. [CrossRef]
19. Splinter, K.D.; Harley, M.D.; Turner, I.L. Remote Sensing Is Changing Our View of the Coast: Insights from 40 Years of Monitoring at Narrabeen-Collaroy, Australia. *Remote Sens.* **2018**, *10*, 1744. [CrossRef]
20. Robinson, D.K.; Mazzucato, M. The Evolution of Mission-Oriented Policies: Exploring Changing Market Creating Policies in the US and European Space Sector. *Res. Policy* **2019**, *48*, 936–948. [CrossRef]
21. Jutz, S.; Milagro-Perez, M.P. Copernicus: The European Earth Observation Programme. *Rev. De Teledetección* **2020**, *56*, V–XI. [CrossRef]
22. Inteti, R.S.; Mandla, V.R.; Peddada, J.R.; Ramesh, N. Analysis of Rice Crop Phenology Using Sentinel-1 and Sentinel-2 Satellite Data. In *Advances in Geotechnical and Transportation Engineering*; Saride, S., Umashankar, B., Avirneni, D., Eds.; Lecture Notes in Civil Engineering; Springer: Singapore, 2020; Volume 71, pp. 257–266, ISBN 9789811536618.
23. Warren, M.A.; Simis, S.G.H.; Martinez-Vicente, V.; Poser, K.; Bresciani, M.; Alikas, K.; Spyrakos, E.; Giardino, C.; Ansper, A. Assessment of Atmospheric Correction Algorithms for the Sentinel-2A MultiSpectral Imager over Coastal and Inland Waters. *Remote Sens. Environ.* **2019**, *225*, 267–289. [CrossRef]
24. Caballero, I.; Fernández, R.; Escalante, O.M.; Mamán, L.; Navarro, G. New Capabilities of Sentinel-2A/B Satellites Combined with in Situ Data for Monitoring Small Harmful Algal Blooms in Complex Coastal Waters. *Sci. Rep.* **2020**, *10*, 8743. [CrossRef]

25. Cabezas-Rabadán, C.; Pardo-Pascual, J.E.; Palomar-Vázquez, J.; Fernández-Sarría, A. Characterizing Beach Changes Using High-Frequency Sentinel-2 Derived Shorelines on the Valencian Coast (Spanish Mediterranean). *Sci. Total Environ.* **2019**, *691*, 216–231. [CrossRef]
26. Yang XiuCheng, Y.X.; Qin QiMing, Q.Q.; Grussenmeyer, P.; Koehl, M. Urban Surface Water Body Detection with Suppressed Built-Up Noise Based on Water Indices from Sentinel-2 MSI Imagery. *Remote Sens. Environ.* **2018**, *219*, 259–270. [CrossRef]
27. Mahammad, S.; Islam, A. Identification of Palaeochannels Using Optical Images and Radar Data: A Study of the Damodar Fan Delta, India. *Arab. J. Geosci.* **2021**, *14*, 1702. [CrossRef]
28. Zuhlke, M.; Fomferra, N.; Brockmann, C.; Peters, M.; Veci, L.; Malik, J.; Regner, P. SNAP (Sentinel Application Platform) and the ESA Sentinel 3 Toolbox. In Proceedings of the Sentinel-3 for Science Workshop, Venice, Italy, 2–5 June 2015; Volume 734, p. 21.
29. Gomarasca, M.A.; Giardino, C.; Bresciani, M.; De Carolis, G.; Sandu, C.; Tornato, A.; Tonolo, F. Copernicus Sentinel Missions for Water Resources. In Proceedings of the Proceedings of 6th International Conference on Space Science and Communication, Johor Bahru, Malaysia, 28–30 July 2019.
30. Pompêo, M.; Moschini-Carlos, V.; Bitencourt, M.D.; Sòria-Perpinyà, X.; Vicente, E.; Delegido, J. Water Quality Assessment Using Sentinel-2 Imagery with Estimates of Chlorophyll a, Secchi Disk Depth, and Cyanobacteria Cell Number: The Cantareira System Reservoirs (São Paulo, Brazil). *Environ. Sci. Pollut. Res.* **2021**, *28*, 34990–35011. [CrossRef] [PubMed]
31. Misra, A.; Balaji, R. Simple Approaches to Oil Spill Detection Using Sentinel Application Platform (SNAP)-Ocean Application Tools and Texture Analysis: A Comparative Study. *J. Indian Soc. Remote Sens.* **2017**, *45*, 1065–1075. [CrossRef]
32. Kyryliuk, D.; Kratzer, S. Evaluation of Sentinel-3A OLCI Products Derived Using the Case-2 Regional CoastColour Processor over the Baltic Sea. *Sensors* **2019**, *19*, 3609. [CrossRef] [PubMed]
33. Su, H.; Liu, H.; Heyman, W.D. Automated Derivation of Bathymetric Information from Multi-Spectral Satellite Imagery Using a Non-Linear Inversion Model. *Mar. Geod.* **2008**, *31*, 281–298. [CrossRef]
34. Stumpf, R.P.; Holderied, K.; Sinclair, M. Determination of Water Depth with High-resolution Satellite Imagery over Variable Bottom Types. *Limnol. Oceanogr.* **2003**, *48*, 547–556. [CrossRef]
35. Lyzenga, D.R. Passive Remote Sensing Techniques for Mapping Water Depth and Bottom Features. *Appl. Opt.* **1978**, *17*, 379–383. [CrossRef] [PubMed]
36. Lyzenga, D.R. Remote Sensing of Bottom Reflectance and Water Attenuation Parameters in Shallow Water Using Aircraft and Landsat Data. *Int. J. Remote Sens.* **1981**, *2*, 71–82. [CrossRef]
37. Lyzenga, D.R.; Malinas, N.P.; Tanis, F.J. Multispectral Bathymetry Using a Simple Physically Based Algorithm. *IEEE Trans. Geosci. Remote Sens.* **2006**, *44*, 2251–2259. [CrossRef]
38. Philpot, W.D. Bathymetric Mapping with Passive Multispectral Imagery. *Appl. Opt.* **1989**, *28*, 1569–1578. [CrossRef]
39. Mateo-Pérez, V.; Corral-Bobadilla, M.; Ortega-Fernández, F.; Vergara-González, E.P. Port Bathymetry Mapping Using Support Vector Machine Technique and Sentinel-2 Satellite Imagery. *Remote Sens.* **2020**, *12*, 2069. [CrossRef]
40. Anne, V.; Jan, J.; Antoine, M.; Thomas, J.; François-Régis, M.-L. New Perspectives in the Monitoring of Marine Sedimentary Transport by Satellites—Advantage and Research Directions. In *Estuaries and Coastal Zones in Times of Global Change*; Nguyen, K.D., Guillou, S., Gourbesville, P., Thiébot, J., Eds.; Springer Water; Springer: Singapore, 2020; pp. 789–808, ISBN 9789811520808.
41. El Islam, B.N.; Fouzia, H.; Khalid, A. Combination of Satellite Images and Numerical Model for the State Followed the Coast of the Bay of Bejaia-Jijel. *Int. J. Environ. Geoinformatics* **2017**, *4*, 1–7. [CrossRef]
42. Houma, F.; Belkessa, R.; Bachari, N.E.I. Contribution of Multispectral Satellite Imagery to the Bathymetric Analysis of Coastal Sea Bottom. *J. Renew. Energ.* **2006**, *9*, 165–172. [CrossRef]
43. Porta, M.; Buosi, C.; Trogu, D.; Ibba, A.; De Muro, S. An Integrated Sea-Land Approach for Analyzing Forms, Processes, Deposits and the Evolution of the Urban Coastal Belt of Cagliari. *J. Maps* **2021**, *17*, 65–74. [CrossRef]
44. Aghdami-Nia, M.; Shah-Hosseini, R.; Rostami, A.; Homayouni, S. Automatic Coastline Extraction through Enhanced Sea-Land Segmentation by Modifying Standard U-Net. *Int. J. Appl. Earth Obs. Geoinf.* **2022**, *109*, 102785. [CrossRef]
45. Wang, Q.; Zhang, Z.; Hao, Z.; Liu, B.; Xiong, J. Optical Classification of Coastal Water Body in China Using Hyperspectral Imagery CHRIS/PROBA. In Proceedings of the IOP Conference Series: Earth and Environmental Science, Beijing, China, 11–13 December 2021; IOP Publishing: Bristol, UK, 2021; Volume 668, p. 012017.
46. McFEETERS, S.K. The Use of the Normalized Difference Water Index (NDWI) in the Delineation of Open Water Features. *Int. J. Remote Sens.* **1996**, *17*, 1425–1432. [CrossRef]
47. Xu, H. Modification of Normalised Difference Water Index (NDWI) to Enhance Open Water Features in Remotely Sensed Imagery. *Int. J. Remote Sens.* **2006**, *27*, 3025–3033. [CrossRef]
48. Rokni, K.; Ahmad, A.; Selamat, A.; Hazini, S. Water Feature Extraction and Change Detection Using Multitemporal Landsat Imagery. *Remote Sens.* **2014**, *6*, 4173–4189. [CrossRef]
49. Zeinali, S.; Talebbeydokhti, N.; Dehghani, M. Spatiotemporal Shoreline Change in Boushehr Province Coasts, Iran. *J. Ocean. Limnol.* **2020**, *38*, 707–721. [CrossRef]
50. Liu, H.; Jezek, K.C. Automated Extraction of Coastline from Satellite Imagery by Integrating Canny Edge Detection and Locally Adaptive Thresholding Methods. *Int. J. Remote Sens.* **2004**, *25*, 937–958. [CrossRef]
51. Kuleli, T.; Guneroglu, A.; Karsli, F.; Dihkan, M. Automatic Detection of Shoreline Change on Coastal Ramsar Wetlands of Turkey. *Ocean Eng.* **2011**, *38*, 1141–1149. [CrossRef]

52. Mukhopadhyay, A.; Mukherjee, S.; Mukherjee, S.; Ghosh, S.; Hazra, S.; Mitra, D. Automatic Shoreline Detection and Future Prediction: A Case Study on Puri Coast, Bay of Bengal, India. *Eur. J. Remote Sens.* **2012**, *45*, 201–213. [CrossRef]
53. Vukadinov, D.; Jovanovic, R.; Tuba, M. An Algorithm for Coastline Extraction from Satellite Imagery. *Int. J. Comput.* **2017**, *2*, 8–15.
54. Ciritci, D.; Türk, T. Automatic Detection of Shoreline Change by Geographical Information System (GIS) and Remote Sensing in the Göksu Delta, Turkey. *J. Indian Soc. Remote Sens.* **2019**, *47*, 233–243. [CrossRef]
55. Yasir, M.; Sheng, H.; Fan, H.; Nazir, S.; Niang, A.J.; Salauddin, M.; Khan, S. Automatic Coastline Extraction and Changes Analysis Using Remote Sensing and GIS Technology. *IEEE Access* **2020**, *8*, 180156–180170. [CrossRef]
56. Ma, Y.; Xu, N.; Liu, Z.; Yang, B.; Yang, F.; Wang, X.H.; Li, S. Satellite-Derived Bathymetry Using the ICESat-2 Lidar and Sentinel-2 Imagery Datasets. *Remote Sens. Environ.* **2020**, *250*, 112047. [CrossRef]
57. Copernicus Browser. Available online: https://browser.dataspace.copernicus.eu/ (accessed on 25 May 2024).
58. Barsi, J.A.; Alhammoud, B.; Czapla-Myers, J.; Gascon, F.; Haque, M.O.; Kaewmanee, M.; Leigh, L.; Markham, B.L. Sentinel-2A MSI and Landsat-8 OLI Radiometric Cross Comparison over Desert Sites. *Eur. J. Remote Sens.* **2018**, *51*, 822–837. [CrossRef]
59. Llorens, R.; Sobrino, J.A.; Fernández, C.; Fernández-Alonso, J.M.; Vega, J.A. A Methodology to Estimate Forest Fires Burned Areas and Burn Severity Degrees Using Sentinel-2 Data. Application to the October 2017 Fires in the Iberian Peninsula. *Int. J. Appl. Earth Obs. Geoinf.* **2021**, *95*, 102243. [CrossRef]
60. Evagorou, E.; Argyriou, A.; Papadopoulos, N.; Mettas, C.; Alexandrakis, G.; Hadjimitsis, D. Evaluation of Satellite-Derived Bathymetry from High and Medium-Resolution Sensors Using Empirical Methods. *Remote Sens.* **2022**, *14*, 772. [CrossRef]
61. Hedley, J.D.; Harborne, A.R.; Mumby, P.J. Technical Note: Simple and Robust Removal of Sun Glint for Mapping Shallow-water Benthos. *Int. J. Remote Sens.* **2005**, *26*, 2107–2112. [CrossRef]
62. Jagalingam, P.; Akshaya, B.J.; Hegde, A.V. Bathymetry Mapping Using Landsat 8 Satellite Imagery. *Procedia Eng.* **2015**, *116*, 560–566. [CrossRef]
63. Louis, J.; Debaecker, V.; Pflug, B.; Main-Knorn, M.; Bieniarz, J.; Mueller-Wilm, U.; Cadau, E.; Gascon, F. Sentinel-2 Sen2Cor: L2A Processor for Users. In Proceedings of the Living Planet Symposium 2016, Prague, Czech Republic, 9–13 May 2016; pp. 1–8.
64. Caballero, I.; Stumpf, R.P. Towards Routine Mapping of Shallow Bathymetry in Environments with Variable Turbidity: Contribution of Sentinel-2A/B Satellites Mission. *Remote Sens.* **2020**, *12*, 451. [CrossRef]
65. Rossi, L.; Mammi, I.; Pelliccia, F. UAV-Derived Multispectral Bathymetry. *Remote Sens.* **2020**, *12*, 3897. [CrossRef]
66. Sherjah, P.Y.; Sajikumar, N. Delineation of Water Body from Sentinel 2 MSI Imagery–a Comparative Study. In Proceedings of the IOP Conference Series: Materials Science and Engineering, Sanya, China, 12–14 November 2021; IOP Publishing, 2021; Volume 1114, p. 012029.
67. Sun, F.; Sun, W.; Chen, J.; Gong, P. Comparison and Improvement of Methods for Identifying Waterbodies in Remotely Sensed Imagery. *Int. J. Remote Sens.* **2012**, *33*, 6854–6875. [CrossRef]
68. Casal, G. Assessment of Sentinel-2 to Monitor Highly Dynamic Small Water Bodies: The Case of Louro Lagoon (Galicia, NW Spain). *Oceanologia* **2022**, *64*, 88–102. [CrossRef]
69. Dahmani, H.; Houma Bachari, F.; Aoudj, C. Modélisation de la dynamique sédimentaire au niveau du port de Cap Djinet, Algérie. In Proceedings of the XVIèmes Journées, Le Havre, France, 9–11 June 2020; Editions Paralia. pp. 205–212.
70. Khalfani, D.; Boutiba, M. Longshore Sediment Transport Rate Estimation near Harbor under Low and High Wave-Energy Conditions: Fluorescent Tracers Experiment. *J. Waterw. Port Coast. Ocean Eng.* **2019**, *145*, 04019015. [CrossRef]
71. Dagorne, A.; Mahrour, M.; Albuisson, M.; Monget, J.-M.; Poisson, M. Télédétection Satellitaire et Cartographie Du Littoral En Algérie. Un Exemple En Kabylie: La Feuille de Djinet. *Méditerranée* **1985**, *54*, 81–94. [CrossRef]
72. Bachari, N.E.I.; Dahmani, H.; Lamri, N.; Mazouzi, M.; Bensari, B.; Houma, F. Contribution of Google Earth and Images from the Sentinel-2 Satellite to the Monitoring of the Silting of Cap Djinet Harbor (Algeria). In *Recent Research on Environmental Earth Sciences, Geomorphology, Soil Science, Paleoclimate, and Karst*; Çiner, A., Khan, M.F., Kallel, A., Rodrigo-Comino, J., Parise, M., Barzegar, R., Ergüler, Z.A., Khelifi, N., Ali, I., Eds.; Advances in Science, Technology & Innovation; Springer Nature: Cham, Switzerland, 2023; pp. 75–77, ISBN 978-3-031-42916-3.
73. Brockmann, C.; Doerffer, R.; Peters, M.; Kerstin, S.; Embacher, S.; Ruescas, A. Evolution of the C2RCC Neural Network for Sentinel 2 and 3 for the Retrieval of Ocean Colour Products in Normal and Extreme Optically Complex Waters. In Proceedings of the Living Planet Symposium, Prague, Czech Republic, 9–13 May 2016; Volume 740, p. 54.
74. Sallaye, M.; Mezouar, K.; Salem Cherif, Y.; Dahmani, A.E.A. Morphological Evolution of Center Boumerdes in Zemmouri Bay (Algeria) from 1922 to 2017. *Arab. J. Geosci.* **2018**, *11*, 602. [CrossRef]
75. Salem Cherif, Y.; Mezouar, K.; Guerfi, M.; Sallaye, M.; Dahmani, A.E.A. Nearshore Hydrodynamics and Sediment Transport Processes along the Sandy Coast of Boumerdes, Algeria. *Arab. J. Geosci.* **2019**, *12*, 800. [CrossRef]
76. Belkessa, R.; Otmani, H.; Mihoubi, M. Impact Du Port de Cap Djinet Sur Le Littoral Est Algérois. In Proceedings of the 4th International Congress Water, Waste & Environment (EDE4), Agadir, Morocco, 18–20 December 2013.
77. Cai, H.; Li, C.; Luan, X.; Ai, B.; Yan, L.; Wen, Z. Analysis of the Spatiotemporal Evolution of the Coastline of Jiaozhou Bay and Its Driving Factors. *Ocean Coast. Manag.* **2022**, *226*, 106246. [CrossRef]